

HAZMAT. VII. The Evolution of Ultraviolet Emission with Age and Rotation for Early M Dwarf Stars

R. O. PARKE LOYD,¹ EVGENYA L. SHKOLNIK,¹ ADAM C. SCHNEIDER,^{2,3} TYLER RICHEY-YOWELL,¹
JAMES A. G. JACKMAN,¹ SARAH PEACOCK,⁴ TRAVIS S. BARMAN,⁴ ISABELLA PAGANO,⁵ AND VICTORIA S. MEADOWS^{6,7}

¹*School of Earth and Space Exploration, Arizona State University, Tempe, AZ 85287*

²*US Naval Observatory, Flagstaff Station, P.O. Box 1149, Flagstaff, AZ 86002, USA*

³*Department of Physics and Astronomy, George Mason University, MS3F3, 4400 University Drive, Fairfax, VA 22030, USA*

⁴*Lunar and Planetary Laboratory, University of Arizona, Tucson, AZ 85721 USA*

⁵*INAF - Osservatorio Astrofisico di Catania, Via S. Sofia 78, 95123, Catania, Italy*

⁶*NASA Astrobiology Institute Alternative Earths and Virtual Planetary Laboratory Teams*

⁷*Department of Astronomy, University of Washington, Seattle, WA, USA*

(Received 2020 September 9; Revised 2020 October 22)

Submitted to The Astronomical Journal

ABSTRACT

The ultraviolet (UV) emission from the most numerous stars in the universe, M dwarfs, impacts the formation, chemistry, atmospheric stability, and surface habitability of their planets. We have analyzed the spectral evolution of UV emission from M0-M2.5 (0.3-0.6 M_{\odot}) stars as a function of age, rotation, and Rossby number, using *Hubble Space Telescope* observations of Tucana Horologium (40 Myr), Hyades (650 Myr), and field (2-9 Gyr) objects. The quiescent surface flux of their C II, C III, C IV, He II, N V, Si III, and Si IV emission lines, formed in the stellar transition region, remains elevated at a constant level for 240 ± 30 Myr before declining by 2 orders of magnitude to field ages. Mg II and far-UV pseudocontinuum emission, formed in the stellar chromosphere, exhibit more gradual evolution with age, declining by 1 and 1.5 orders of magnitude, respectively. The youngest stars exhibit a scatter of 0.1 dex in far-UV line and pseudocontinuum flux attributable only to rotational modulation, long-term activity cycles, or an unknown source of variability. Saturation-decay fits to these data can predict an M0-M2.5 star's quiescent emission in UV lines and the far-UV pseudocontinuum with an accuracy of 0.2-0.3 dex, the most accurate means presently available. Predictions of UV emission will be useful for studying exoplanetary atmospheric evolution, the destruction and abiotic production of biologically relevant molecules, and interpreting infrared and optical planetary spectra measured with observatories like the *James Webb Space Telescope*.

1. INTRODUCTION

Randomly pick an Earth-sized planet in the universe and, more likely than not, it will orbit an M dwarf star. This is true also if one were to draw a planet only from those in the classical “habitable zone,” the region of planetary orbits where liquid water is possible on the surface of an Earth-like planet (Kasting et al. 1993; Kopparapu et al. 2013). This conclusion comes from the fact that M dwarfs outnumber Sun-like stars by a factor of roughly 20 (Henry et al. 2018) and that, on average, an M dwarf will have more Earth-sized planets than an F,

G, or K star (Mulders 2018). The space environment of M dwarfs is much different than that of the most familiar planetary system, the Solar System. Their fractional X-ray and ultraviolet (UV) emission exceeds the Sun's by up to two orders of magnitude (Lloyd et al. 2016), and these stars experience a comparatively prolonged period of even more elevated emission in their youth (Shkolnik & Barman 2014).

An M dwarf's high energy photons make up only a small fraction of its total luminosity, yet they can shape a planet's atmosphere. UV and X-ray photons break atom-atom and atom-electron bonds, chemically modifying, heating, desiccating, and evaporating planetary atmospheres and oceans (e.g., Hu et al. 2012; Luger et al. 2015). Understanding the evolution of this radiation as

these stars age is necessary to understand the evolution and present state of their planets. This includes interpreting the spectra of planets, such as those soon to be observed in the optical and infrared by the next generation of ground and space-based telescopes (NAS Exoplanet Science Strategy Report 2018¹).

Individual emission lines in the UV are important to both planetary and stellar physics. The photolysis cross sections for molecules are heavily wavelength dependent (e.g., Segura et al. 2005). Because of this, spectrally-resolved UV input is essential to photochemical models of exoplanetary atmospheres. UV emission lines can also be a tool to guide physical models of stellar upper atmospheres that in turn can predict important regions of stellar emission that have not or cannot be observed, such as extreme UV (EUV) emission absorbed by intervening gas in the interstellar medium (ISM) (Fontenla et al. 2016; Peacock et al. 2020; see also Section 6.5). The utility of UV lines in constraining models comes from the fact that various lines within the UV band include significant emission from chromospheric, transition region, coronal, and even photospheric plasma. In the same vein, UV spectra have been used in differential emission measure analyses to predict optically thin emission in the EUV (e.g., Pagano et al. 2000).

In this work, we present observations of the UV spectral evolution of early M stars² with age. This is the latest in a body of work from the HAbitable Zones and M dwarf Activity across Time (HAZMAT) program. Earlier work by the HAZMAT program leveraged archival data from the *GALEX* and *ROSAT* missions to measure changes in the broadband near-UV (NUV), far-UV (FUV), and X-ray emission of M stars (Shkolnik & Barman 2014; Schneider & Shkolnik 2018), and combined these data with sophisticated atmospheric models to reconstruct the evolution of M star EUV emission (Peacock et al. 2020). The program has also investigated the time variability of UV emission on minute to year timescales (Miles & Shkolnik 2017), including temporally and spectrally resolved UV observations of flares on 40 Myr M stars (Loyd et al. 2018a). Richey-Yowell et al. (2019) recently extended HAZMAT into an investigation of K star activity evolution. New *Hubble Space Telescope* (*HST*) observations to deepen this investigation are underway (program 15955, PI Richey-Yowell).

Beyond the HAZMAT program, most studies of M dwarf activity in recent decades have primarily focused on H α and X-ray emission as a function of rotation (Stauffer et al. 1997; Delfosse et al. 1998; Pizzolatto et al. 2003; Wright et al. 2011, 2018). The age evolution of X-ray emission has been addressed by Feigelson et al. (2004); Preibisch & Feigelson (2005); and Jackson et al. (2012). In the most closely related study outside of the HAZMAT program, Stelzer et al. (2013) (erratum: Stelzer et al. 2014) examined the X-ray and broadband UV emission of a 10 pc sample of M dwarfs, fitting an unbroken power law to the age evolution of their emission. This paper is the first look into the age evolution of specific chromospheric and transition-region UV emission lines for early M stars.

2. OBSERVATIONS AND STELLAR SAMPLE

The HAZMAT *HST* survey (program ID 14784, PI Shkolnik) collected data using the Cosmic Origins Spectrograph (COS; Green et al. 2012) with the G130M and G160M ($R = 12,000$ - $20,000$) and G230L ($R = 2,000$ - $4,000$) gratings. Observations were made of 21 M stars, 12 from the Tucana-Horologium (Tuc-Hor; 40 Myr; Kraus et al. 2014) moving group, 6 from the Hyades cluster (650 Myr; Martín et al. 2018), and 3 unassociated field stars (2-10 Gyr).

We incorporate some additional data from the *HST* archive. The field stars build upon the archival sample of 4 objects from the MUSCLES Treasury survey for a total of 7 field stars (Measurements of the Ultraviolet Spectral Characteristics of Low-mass Exoplanetary Systems Treasury survey; program IDs 12464 and 13650; PI France; France et al. 2016; Youngblood et al. 2016; Loyd et al. 2016). We also included archival data from programs 14767 (PI Sing; dos Santos et al. 2019) and 15174 (PI Loyd) for one of the 7 field stars, GJ 436. Table 1 gives parameters of the stellar sample and Table 2 summarizes the observations. Note that the FUV and NUV observations, while often closely spaced in time, are not simultaneous. We retrieved *K2* and *TESS* light curves for all targets from the Mikulski Archive for Space Telescopes (MAST³) where available at the time of analysis to measure rotation periods. The *HST* data described here may be obtained from the MAST archive through a single DOI portal at [doi:10.17909/t9-se6p-dn04](https://doi.org/10.17909/t9-se6p-dn04).

The stellar sample is limited to subtypes M0-M2.5, with the exception of three stars possibly in the M2.5-M3.5 range, to minimize variations due to differences in stellar properties. This roughly corresponds to masses

¹ <https://www.nap.edu/catalog/25187/exoplanet-science-strategy>

² Throughout this work, we generally use the term “M star” as opposed to “M dwarf” to encompass young objects that have not yet fully contracted onto the main sequence.

³ <https://archive.stsci.edu>

Table 1. Properties of the stellar sample.

Group	Star	2MASS Designation	Spectral Type	Ref	Alternate Type ^a	T_{eff}^b K	Radius R_{\odot}	Age Myr	P_{rot}^c d	Ref	R_o	[FeH]	Ref	Distance ^d pc
Tuc-Hor	J03315	J03315564-4359135	M0.0 ± 0.6	1	K5.2 ± 1	3959 ± 80	0.824 ± 0.087	40 ± 5	2.92 ± 0.01 ^e	2	0.089	45.275 ± 0.071
	J00240	J00240899-6211042	M0.2 ± 0.9	1	K7.2 ± 1	3777 ± 80	0.858 ± 0.091	40 ± 5	1.76 ± 0.03 ^e	3	0.044	44.2 ± 1.1
	J02543	J02543316-5108313	M1.4 ± 0.7	1	M1.1 ± 1	3563 ± 80	0.828 ± 0.088	40 ± 5	43.76 ± 0.21
	J23261	J23261069-7323498	M1.5 ± 1	1	K7.7 ± 1	3762 ± 80	0.740 ± 0.078	40 ± 5	0.57 ± 0.01 ^e	3	0.014	46.294 ± 0.059
	J01521	J01521830-5950168	M1.6 ± 0.4	1	M1.6 ± 1	3531 ± 80	0.656 ± 0.069	40 ± 5	6.35 ± 0.06 ^e	2	0.12	39.765 ± 0.040
	J00393	J00393579-3816584	M1.8 ± 0.4	1	M1.4 ± 1	3555 ± 80	0.693 ± 0.073	40 ± 5	6.32	4	0.12	40.241 ± 0.070
	J02001	J02001277-0840516	M2.0 ± 0.2	1	M2.1 ± 1	3480 ± 80	0.662 ± 0.070	40 ± 5	1.75	5	0.029	36.926 ± 0.069
	J02365	J02365171-5203036	M2	6	...	3504 ± 80	0.809 ± 0.086	40 ± 5	0.74 ± 0.01 ^e	3	0.013	38.847 ± 0.051
	J22025	J22025453-6440441	M2.1 ± 0.6	1	M1.8 ± 1	3525 ± 80	0.678 ± 0.072	40 ± 5	0.43 ± 0.01 ^e	3	0.0073	43.705 ± 0.098
	J23285	J23285763-6802338	M2.9 ± 0.5	1	M2.3 ± 1	3444 ± 80	0.666 ± 0.070	40 ± 5	0.74	5	0.012	46.048 ± 0.050
Hyades	J22463	J22463471-7353504	M3.2 ± 0.3	1	M2.3 ± 1	3451 ± 80	0.609 ± 0.064	40 ± 5	1.65 ± 0.01 ^e	3	0.027	50.224 ± 0.074
	J02125	J02125819-5851182	M3.5 ± 0.5	1	M1.9 ± 1	3513 ± 80	0.671 ± 0.071	40 ± 5	1.60	3	0.028	48.061 ± 0.049
	HAN 192	J04184702+1321585	M0.5 ± 0.5	3	...	3922 ± 88	0.624 ± 0.086	650 ± 70	14 ± 4	3	0.39	0.146 ± 0.004	7	46.14 ± 0.16
	TYC 1265	J04260470+1502288	M1 ± 0.5	3	...	3901 ± 88	0.601 ± 0.082	650 ± 70	16 ± 5	3	0.43	0.146 ± 0.004	7	47.88 ± 0.22
	LP 415	J04363893+1836567	M2 ± 0.5	3	...	3580 ± 88	0.463 ± 0.064	650 ± 70	21.9	8	0.40	0.146 ± 0.004	7	42.109 ± 0.084
	LP5-282	J04225989+1318585	M2 ± 0.5	3	...	3588 ± 88	0.491 ± 0.067	650 ± 70	9 ± 2	3	0.16	0.146 ± 0.004	7	53.29 ± 0.13
	REID 176	J04223953+1816097	M2 ± 0.5	3	...	3629 ± 88	0.489 ± 0.067	650 ± 70	23.124 ± 0.009 ^e	9	0.44	0.146 ± 0.004	7	41.707 ± 0.094
	GJ 3290	J04271663+1714305	M2 ± 0.5	3	...	3663 ± 88	0.511 ± 0.070	650 ± 70	0.146 ± 0.004	7	45.990 ± 0.098
	GJ 176	J04425581+1857285	M2.0	10	...	3591 ± 98	0.480 ± 0.060	2200 ⁺⁸⁴⁰⁰ ₋₁₀₀	39.3 ± 0.1 ^e	11	0.72	0.15	12	9.4730 ± 0.0063
	GJ 436	J11421096+2642251	M2.5	13	...	3464 ± 101	0.424 ± 0.046	2400 ⁺⁴²⁰⁰ ₋₂₀₀	44.09 ± 0.08 ^e	14	0.74	-0.0 ± 0.2	15	9.7560 ± 0.0089
Field	GJ 832	J21333397-4900323	M1.5	16	...	3584 ± 86	0.443 ± 0.046	4800 ⁺⁵⁸⁰⁰ ₋₂₀₀₀	46 ± 9	11	0.59	-0.3 ± 0.2	17	4.9651 ± 0.0011
	G75-55	J02582009-0059330	M1	18	...	3793 ± 88	0.562 ± 0.063	4800 ⁺⁵²⁰⁰ ₋₃₆₀₀	-0.10 ± 0.12	18	23.896 ± 0.050
	LTT 2050	J04374188-1102198	M2.5 ± 0.5	3	...	3615 ± 102	0.459 ± 0.053	8600 ⁺³⁷⁰⁰ ₋₄₈₀₀	62	19	1.2	0.10 ± 0.12	18	11.2144 ± 0.0039
	GJ 3997	J17155010+1900000	M1	18	...	3713 ± 74	0.425 ± 0.033	8700 ⁺⁴⁰⁰⁰ ₋₅₄₀₀	-0.25 ± 0.12	18	13.058 ± 0.035
	GJ 667C	J17185868-3459483	M1.5	20	...	3489 ± 58	0.322 ± 0.020	8700 ⁺³⁴⁰⁰ ₋₄₄₀₀	103.9 ± 0.7 ^e	11	2.1	-0.6 ± 0.1	20	7.2455 ± 0.0048

^a Alternate spectral type determination from Kraus et al. (2014) based on optical spectral indices. The types from Kraus et al. (2014) of the previous column are based on SED fitting.

^b Stellar effective temperature.

^c Rotation period.

^d From GAIA (Gaia Collaboration et al. 2018).

^e Period uncertainty excluded from analysis (see Section 2).

References—(1) Kraus et al. 2014; (2) Messina et al. 2011; (3) This Work; (4) Watson et al. 2006; (5) Oelkers et al. 2018; (6) Torres et al. 2006; (7) Cummings et al. 2017; (8) Douglas et al. 2019; (9) Douglas et al. 2016; (10) Forveille et al. 2009; (11) Suárez Mascareño et al. 2015; (12) von Braun et al. 2014; (13) Butler et al. 2004; (14) Bourrier et al. 2018; (15) Torres et al. 2008; (16) Bailey et al. 2009; (17) Wittenmyer et al. 2014; (18) Gaidos et al. 2014; (19) Astudillo-Defru et al. 2017; (20) Anglada-Escudé et al. 2013

NOTE—See Section 2 for details on stellar parameters estimated in this work as well as the adopted ages.

of 0.3-0.6 M_{\odot} (Baraffe & Chabrier 1996). Kraus et al. (2014) derived spectral types for all but one of the Tuc-Hor objects using both SED fitting and optical spectral indices. Three Tuc-Hor objects could be K stars according to optical indices, but the inclusion or exclusion of these objects from the analysis has no significant effect (see Section 5). For the Hyades and field targets, wherever possible we assigned types ourselves for stars that had spectra from the ELODIE archive at the Observatoire de Haute-Provence (OHP; Moutaka et al. 2004)⁴, matched against SDSS standards (Bochanski et al. 2007). Although the stellar samples from each age group are matched in spectral type, the average mass of the Tuc-Hor group is likely a few 0.01 M_{\odot} above that of the Hyades and Field groups because of their pre-main-sequence position on the HR diagram (D’Antona & Mazzitelli 1994). We intentionally did not select targets on the basis of existing planets to avoid introducing a bias toward lower activity levels that favor planet detection. These stars represent a subsample of the stars included in the UV activity evolution analysis of Shkolnik & Barman (2014), which used data from the *GALEX* survey covering most of the sky. The stars in the present sample cover a representative range of UV activity levels of M stars at large.

The age of stars in the Tuc-Hor group has been estimated through isochrone fitting, with specific attention paid to the poor performance of stellar structure models at young ages for early types, to be 45 ± 4 Myr (Bell et al. 2015). This agrees fairly well with a constraint on the age of 35-45 Myr placed by a lithium depletion argument (Kraus et al. 2014). The H α emission of these stars is also consistent with a young age (Kraus et al. 2014). We use an age of 40 ± 5 Myr in this work

The age of the Hyades cluster has been estimated using isochrone and gyrochrone fitting as 700 Myr (Maeder & Mermilliod 1981), 625 ± 25 Myr (Perryman et al. 1998), and 750 ± 100 Myr (Brandt & Huang 2015). Recently, Martín et al. (2018) extended the Li depletion boundary method to brown dwarf masses to derive an age of 650 ± 70 Myr for the Hyades. For this work, we adopt an age of 650 ± 70 Myr. The range of possible ages for both the Hyades and Tuc-Hor stars is small relative to the > 2 orders of magnitude in age spanned by the full stellar sample.

We computed age estimates for the field stars based on combined isochrone and gyrochrone fitting via the stardate package (Angus et al. 2019b). For this, we provided stardate with *Gaia* (Gaia Collaboration

et al. 2018) and *2MASS* (Cutri et al. 2003) magnitudes for each field star, along with the rotation periods where available. The derived ages have uncertainties of several Gyr, as shown in Table 1. Such large uncertainties are reasonable given that the rotational evolution of K and M stars is an area of active study, with evidence for complicating variations in the rate of spin-down with age (Newton et al. 2016, 2018; Curtis et al. 2019; Spada & Lanzafame 2020; Curtis et al. 2020).

Table 2. Summary of observations.

Star	Grating	T_{exp}^a (ks)	First Observation	Last Observation
J03315	G130M	10.1	2017-07-20	2017-07-20
	G160M	10.8	2017-07-19	2017-07-20
	G230L	4.6	2017-07-19	2017-07-19
J00240	G130M	1.6	2017-08-30	2017-08-30
	G160M	1.5	2017-08-30	2017-08-30
	G230L	0.3	2017-08-30	2017-08-30
J02543	G130M	1.4	2017-08-12	2017-08-12
	G160M	1.0	2017-08-12	2017-08-12
	G230L	0.4	2017-08-12	2017-08-12
J00393	G130M	1.3	2017-09-21	2017-09-22
	G160M	1.5	2017-09-21	2017-09-21
	G230L	0.6	2017-09-21	2017-09-21
J23261	G130M	1.4	2017-08-18	2017-08-18
	G160M	1.4	2017-08-18	2017-08-18
	G230L	0.6	2017-08-18	2017-08-18
J01521	G130M	1.3	2017-08-17	2017-08-17
	G160M	1.5	2017-08-17	2017-08-17
	G230L	0.3	2017-08-17	2017-08-17
J22025	G130M	1.3	2017-08-30	2017-08-30
	G160M	1.3	2017-08-30	2017-08-30
	G230L	0.3	2017-08-30	2017-08-30
J02125	G130M	1.8	2017-10-04	2017-10-04
	G160M	0.7	2017-10-04	2017-10-04
	G230L	0.3	2017-10-04	2017-10-04
J02365	G130M	10.0	2017-08-09	2017-08-09
	G160M	10.9	2017-08-08	2017-08-08
	G230L	1.8	2017-08-08	2017-08-08
J02001	G130M	1.8	2017-08-31	2017-08-31
	G160M	0.9	2017-08-31	2017-08-31
	G230L	0.4	2017-08-31	2017-08-31
J23285	G130M	1.3	2017-08-19	2017-08-19
	G160M	1.5	2017-08-18	2017-08-19
	G230L	0.3	2017-08-18	2017-08-18
J22463	G130M	2.3	2017-09-01	2017-09-01
	G160M	1.5	2017-09-01	2017-09-01

⁴ <http://atlas.obs-hp.fr/elodie/>

Table 2 continued

Table 2 (*continued*)

Star	Grating	T_{exp}^a (ks)	First Observation	Last Observation
TYC 1265	G230L	0.6	2017-09-01	2017-09-01
	G130M	10.4	2018-08-22	2018-08-22
	G160M	10.8	2018-08-20	2018-08-20
HAN 192	G230L	2.2	2018-08-20	2018-08-20
	G130M	12.2	2018-12-02	2019-03-30
	G160M	10.8	2018-11-29	2018-11-29
LP5-282	G230L	2.2	2018-11-29	2018-11-29
	G130M	7.6	2018-02-28	2018-02-28
	G160M	10.8	2018-02-27	2018-02-27
REID 176 ^b	G230L	2.3	2018-02-27	2018-02-27
	G230L	20.8	2018-03-20	2018-12-15
	G130M	21.4	2017-09-29	2017-09-30
GJ 3290	G160M	21.4	2017-09-27	2017-09-27
	G230L	5.4	2017-09-26	2017-09-26
	G130M	21.4	2017-09-06	2017-09-07
LP 415	G160M	21.4	2017-09-05	2017-09-06
	G230L	5.4	2017-09-05	2017-09-05
	G130M	12.6	2015-03-02	2015-03-02
GJ 176	G160M	5.6	2015-02-28	2015-02-28
	G230L	5.8	2013-09-07	2015-02-28
	G130M	81.1	2012-06-23	2018-02-28
GJ 436	G160M	9.5	2012-06-23	2015-06-25
	G230L	4.0	2015-06-25	2015-06-25
	G130M	15.1	2012-07-28	2014-10-11
GJ 832	G160M	7.7	2012-07-28	2014-10-10
	G230L	2.8	2014-10-10	2014-10-10
	G130M	11.6	2017-10-16	2018-11-04
G75-55	G160M	4.5	2017-10-16	2018-11-04
	G230L	0.7	2017-10-16	2017-10-16
	G130M	12.6	2017-10-17	2018-11-03
LTT 2050	G160M	7.5	2017-10-17	2018-07-14
	G230L	0.7	2017-10-17	2017-10-17
	G130M	2.3	2017-09-18	2017-09-18
GJ 3997	G160M	1.3	2017-09-18	2017-09-18
	G230L	0.7	2017-09-18	2017-09-18
	G130M	4.6	2015-08-07	2015-08-07
GJ 667C	G160M	4.5	2015-08-07	2015-08-07
	G230L	2.5	2015-08-07	2015-08-07

^aCumulative exposure time.

^bNot observed with G130M or G160M gratings due to detector flare safety restrictions.

NOTE—Most observations are from program 14784 (PI Shkolnik). Observations of GJ 176, GJ 436, GJ 832, and GJ 667C are from programs 12464 and 13650 (PI France), with additional observations of GJ 436 from programs 14767 (PI Sing) and 15174 (PI Loyd).

For consistency and completeness, we estimated the effective temperature (T_{eff}) and radii (R) of the sam-

ple stars from *Gaia* photometry, expanding upon the procedure from Curtis et al. (2020). We calibrated the relationships between T_{eff} , *Gaia* G -band (4,000-10,000 Å) surface flux, and *Gaia* $BP - RP$ color (4,000-6,500 and 6,500-10,000 Å) for the well-characterized M dwarf sample of Mann et al. (2015). Applying this relationship to the $BP - RP$ colors of the sample stars yielded T_{eff} and G -band surface fluxes. Using the measured G -band fluxes, we then derived a photometric radius for the star. For stars in the 40 Myr Tuc-Hor association, these photometric radii exceed those predicted by MIST stellar models (Dotter 2016; Choi et al. 2016) by 10-60%. Stellar evolution models are sensitive to formulations of opacity, convection, and boundary conditions, among other details, yielding inaccurate isochronal ages for young stellar groups (Bell et al. 2015). Therefore, we prioritize the photometric radii.

To obtain rotation periods for each star, we located *TESS* photometry wherever possible and conducted a Lomb-Scargle analysis, validating all periods by eye. We also conducted a literature search for rotation period measurements. This resulted in rotation period measurements for every star except GJ 3997, G75-55, and GJ 3290. These stars have been observed by either *TESS* or *K2*, but no rotational modulation was apparent in their light curves.

Where there was overlap, literature periods generally agreed with our analysis of *TESS* data. However, we encountered a few exceptions. For J23285, Oelkers et al. (2018) measured a period of 0.74 d whereas we obtained a rotation period at the second harmonic of 0.37 d from *TESS* photometry. We selected the 0.74 d period as more consistent with the star’s emission line broadening (with the caveat that narrower lines could be due to a pole-on inclination). The opposite occurred for J22463, where Oelkers et al. (2018) measured a period of 0.299 d while we measured a period of 1.65 d, and we selected our measurement as, again, more consistent with the star’s emission line broadening as well as the *TESS* lightcurve. Several discrepant values have been measured for J02365, namely 2.93 d (Oelkers et al. 2018), 1.54 d (Messina et al. 2010), 0.74 d (Watson et al. 2006), and 0.74 d (this work). We chose 0.74 d since this is the only value for which two measurements agree and this period is clear in the *TESS* lightcurve (Appendix B). Since these discrepant rotation periods are all well within the saturated activity regime (Section 5), these choices ultimately have no impact on our analysis.

The rotation period discrepancies highlight the fact that such measurements are always subject to the possibility that the true period is a harmonic of the one identified. For this reason, high precisions on quoted

periods can lead to a false sense of accuracy. As high precisions do not improve our analysis, we omitted uncertainties on periods in our analysis where they were below 5%. We retain larger uncertainties, such as that of TYC 1265, as they have the potential to significantly increase uncertainty in the fits of Section 4.2.

Rossby number, the ratio of a star’s rotation period to the timescale for convective turnover in its interior, $Ro = P_{\text{rot}}/\tau_c$, is often used as a proxy for a star’s magnetic activity (Noyes et al. 1984). As stars age and spin down, their Rossby numbers increase. There is no method to measure a star’s convective turnover timescale. Instead, τ_c must be estimated theoretically (e.g., Kim & Demarque 1996) or empirically by seeking a form for τ_c as a function of stellar mass or color that minimizes scatter in fits to stellar activity decay (e.g., Noyes et al. 1984). Prescriptions for τ_c can vary by factors of a few (Brandenburg 2020), and without a means of directly measuring τ_c , it is impossible to assess the true accuracy of any such prescription. Nonetheless, τ_c remains useful as a tool to predict the quiescent activity level for a star of arbitrary mass and rotation rate so long as the prescription used for τ_c is kept consistent.

We used the prescription of Wright et al. (2018) to compute τ_c from $V - K_S$ colors for the stars in this work. The empirical Wright et al. (2018) relationship is constrained by roughly 300 objects within the same color range as the present sample, including young, fully convective objects. We obtained V photometry for the targets from Zacharias et al. (2012) and K photometry from Cutri et al. (2003). Scatter in the Wright et al. (2018) relationship is at the 0.05 dex level.

3. DATA REDUCTION

For each dataset, we used the method of Loyd et al. (2018b) to identify flares and anomalies in light curves of the band integrated flux measured by each instrument configuration, excluding regions contaminated by emission from Earth’s geocorona. We then extracted integrated spectra using calCOS v3.3.9 excluding these time ranges to obtain “quiescence only” spectra. An analysis of these flares has already been published for the Tuc-Hor sample (Loyd et al. 2018a) and flares in the remainder of the sample will be the subject of a future work. These spectra might not represent a true quiescence, as unresolved flares could still be present. However, we estimated from the flare frequency distribution of Loyd et al. (2018b) that flares below a typical detection limit for the data would contribute on average < 10% (< 0.04 dex) to the time-integrated flux.

Small offsets in the wavelength solution of a few km s^{-1} are possible between COS exposures (Linsky

et al. 2010). To mitigate these offsets, we applied kernel density estimation to the wavelength calibrated detector events to identify the peaks of the lines in Table 3. From these, we determined the offset necessary to shift the wavelength solution of the exposure to the stellar rest frame. We chose this method versus cross-correlation out of concern that a cross-correlation method would perform poorly for exposures where emission lines represented only a few counts above the background and background noise dominated over most of the spectrum. Applying these shifts in a second run of calCOS generated “wavelength-corrected” spectra.

The calCOS pipeline adds a conservative zero-point error to the fluxed spectrum from each exposure. When the pipeline coadds dithered exposures, these zero-point errors accumulate to unrealistic levels. For more accurate errors in coadded spectra, we subtracted (in quadrature) a constant offset in the error such that the final error on the band-integrated spectrum matched that of the Poissonian error, effectively removing the zero-point offset.

The calCOS pipeline will not coadd spectra obtained using differing central wavelength settings. Differing central wavelengths shift COS spectra by up to a few tens of Å. Where necessary, we coadded spectra obtained with the same grating at different central wavelength settings using an in-house code described in Appendix A. This was the final step in our data reduction process and yielded spectra comprised of all available data, shifted to the rest frame of the star, and with no measurable contribution from flares.

4. ANALYSIS

4.1. Line and Pseudocontinuum Fluxes

The strongest lines in the COS spectra not contaminated by geocoronal emission are C III, Si III, N V, C II, Si IV, C IV, He II, and Mg II. Table 3 provides the wavelengths and peak formation temperatures of these lines. We fit the components of each of these lines with double Voigt profiles convolved with the COS line spread function (LSF) and a constant offset for the underlying continuum using the affine-invariant Markov Chain Monte Carlo (MCMC) software emcee (Foreman-Mackey et al. 2013). Single Voigt profiles did not capture broad wings at the base of the lines, even when convolved with the COS LSF, whereas including two components yielded a satisfactory fit to both the peak and wings of the lines. For multiplets, we held the widths of the line components fixed between members of the multiplet but allowed their flux ratios to vary freely. We fit the He II multiplet as a single line using average parameters

Table 3. Emission lines fit in analysis.

Ion	$\lambda_{\text{rest}} \text{ \AA}$	$\log_{10}(T_{\text{peak}}/\text{K})^a$
C III	1174.93	4.7
	1175.26	4.7
	1175.59	4.7
	1175.71	4.7
	1175.99	4.7
	1176.37	4.7
Si III	1206.51	4.7
N V	1238.82	5.2
	1242.80	5.2
C II	1334.53	4.5
	1335.71	4.5
Si IV	1393.76	4.9
	1402.77	4.9
C IV	1548.20	4.8
	1550.77	4.8
He II ^b	1640.4	4.9
Mg II	2796.35	3.6-4.0
	2803.53	3.6-4.0
Integration Bands (\AA)		
FUV	1160-1172, 1250-1290, 1320-1330,	
Pseudo-	1340-1390, 1406-1540,	
continuum	1590-1635, 1680-1740	

^aC line formation temperatures are line center values from [Avrett & Loeser \(2008\)](#), the Mg II range is from [Leenaarts et al. \(2013\)](#), and the remainder are from the [CHIANTI database \(Dere et al. 2009\)](#).

^bUnresolved multiplet.

(weighted by oscillator-strength) because these lines are naturally unresolved.

Low S/N data often yielded implausible line widths far different from the high S/N data. Therefore, we used the fits from high S/N data to guide priors on line widths that we applied to all fits. We specified a uniform prior on the combined thermal and turbulent broadening, $\sqrt{2kT/m + v_{\text{turb}}^2}$, of the fit between 20 and 100 km s⁻¹ for the narrow line component and a uniform prior between 100 and 500 km s⁻¹ for the broad component. We appended a Gaussian tail with $\sigma = 5$ km s⁻¹ to the 20 km s⁻¹ end of the boxcar prior for the narrow component and a Gaussian tail with $\sigma = 50$ km s⁻¹ to the 500 km s⁻¹ end of the prior for the broad component.

Several C II lines showed absorption from the ISM in the blue component of the doublet, since this is formed by transitions from the ground level. We fit for this absorption with a single narrow absorption line profile. The MCMC sampler often jumped to parameters that

provided a reasonable fit to most of the data, but missed the ISM absorption. To avoid this, we specified a uniform probability that the ISM absorption was centered within 30 km s⁻¹ of the stellar rest frame, including $\sigma = 5$ km s⁻¹ Gaussian tails on either end of this range. We also required that the broadening of the ISM line be less than 10 km s⁻¹ based on the ISM observations of [Redfield & Linsky \(2002\)](#).

We observed Mg II emission with the G230L grating, which leaves structure below about 30 km s⁻¹ in the lines unresolved. This includes intrinsic line widths below 30 km s⁻¹, a self-reversed core, or ISM absorption ([Redfield & Linsky 2002](#)). We examined the fits and confirmed that the total flux from the line fits, the key parameter for this study, agrees with a simple integration of the data. Hence, narrow line widths or self absorptions not captured by the fits did not impact our results. The possibility of ISM absorption could impact the intrinsic flux we measured, meriting a more careful treatment that is discussed in Section 6.2.

Figure 1 plots example C II and Mg II line fits from the sample. Parameters of the fits and MCMC chains for each line of each star are available from the corresponding author upon request.

In addition to line fluxes, we computed the flux from FUV pseudocontinuum regions between these lines through simple integration. We use the term pseudocontinuum to deliberately acknowledge that these regions consist primarily of unresolved lines and ionization edges rather than blackbody emission ([Peacock et al. 2019](#)). The wavelengths across which we integrated the FUV pseudocontinuum are listed in Table 3.

4.2. Evolution of Emission Lines

We fit an empirical model to the quiescent activity evolution of the stars as a function of age, rotation period, and Rossby number, again using *emcee* ([Foreman-Mackey et al. 2013](#)). The form of the model was a constant saturation followed by a power law decline,

$$F = \begin{cases} F_{\text{sat}}, & x \leq x_{\text{sat}} \\ F_{\text{sat}} (x/x_{\text{sat}})^{-\alpha}, & x > x_{\text{sat}} \end{cases} \quad (1)$$

where x stands in for age, rotation period, or Rossby number and the free parameters are the saturation surface flux, F_{sat} ; end of saturation, x_{sat} ; and power-law index, α . We included a hyperparameter, σ , to describe a uniform Gaussian scatter about the fit in log space.

The three age groups of the data do not resolve the transition from saturation to declining activity. This lifetime has been probed by a number of previous studies using H α , UV, and X-ray observations ([West et al. 2008](#); [Jackson et al. 2012](#); [Shkolnik & Barman 2014](#); [John-](#)

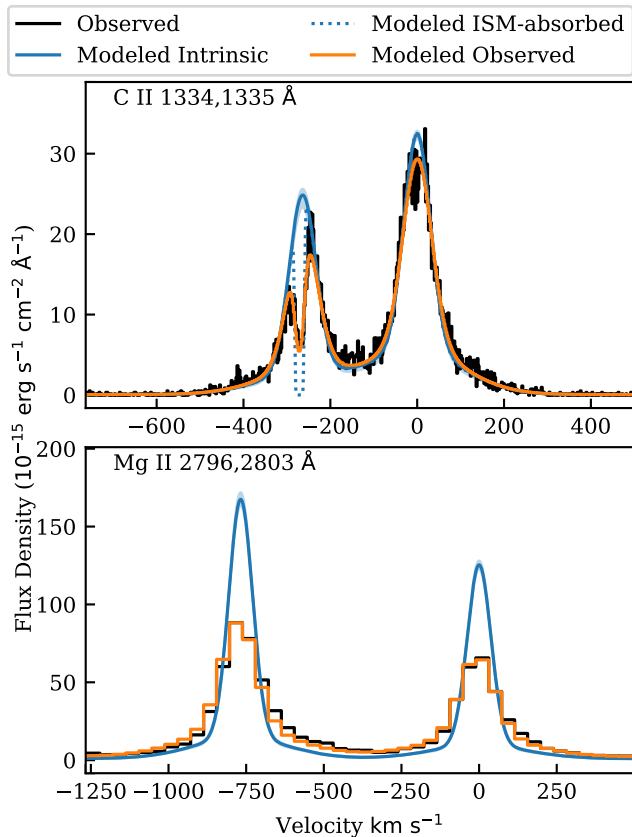


Figure 1. Example fits to two UV lines for the star J02365 using the superposition of two Voigt profiles for each component of the doublet. Top: C II lines exhibiting clear ISM absorption in the blueward line. These are well-resolved by the COS G130M grating ($R \approx 15,000$). Bottom: Mg II lines. The COS G230L grating ($R \approx 3,000$) used for these observations significantly broadens the intrinsic line profiles and weakens their peaks. ISM absorption affects Mg II (see Section 6.2), but we did not model any absorption since it was not resolved. The Mg II lines are the only strong UV lines included in the analysis that were not resolved.

stone et al. 2020). McDonald et al. (2019) fit *ROSAT* X-ray data compiled by Shkolnik & Barman (2014) using MCMC methods, yielding a posterior distribution on the duration of the saturated period that ranges from 100 to 500 Myr at the 16th and 84th percentiles and favors 400 Myr. Because age was sparsely sampled by the HAZMAT *HST* program, we applied this posterior as a prior on saturation lifetime in our MCMC fits. However, doing so yielded a statistically insignificant change in the best-fit value of the saturation lifetime relative to an uninformative prior, indicating that even with sparse age sampling the HAZMAT data constrain the activity saturation lifetime for early M stars. In fitting quiescent activity vs. rotation period or Rossby number, rather than age, we applied no prior on saturation lifetime.

We included uncertainties in age, rotation period (when significant), and Rossby number in this analysis by computing the data likelihood as an integral of the probability over the path of the model. Systematic errors in the determination of the convective turnover time could lead to additional uncertainty in Rossby number that we did not include (see Section 2).

5. RESULTS

Spectra of representative stars from each age group are shown in Figure 2, cast in luminosity, surface flux, and a “rotation-normalized” surface flux, further explained in Section 6. For visual comparison, we split these spectra into continuum regions and strong emission lines and excluded regions contaminated by Earth’s geocoronal emission (namely, the Ly α and O I lines). We replaced the emission lines with their double-Voigt profiles from MCMC fits with instrumental broadening removed. We also removed ISM absorption from the blueward C II line. For the regions between these lines, we binned to 10 Å for higher S/N. The spectra consist of data from the COS G130M and G160M gratings ($R = 12,000$ -20,000) up to roughly 1750 Å, beyond which the data originate from the G230L grating ($R = 2,000$ -4,000). For many spectra, this results in a jump to higher noise levels redward of 1750 Å, yielding a nondetection of the continuum represented in the figure as dotted lines giving 2σ upper limits. The G230L mode does not capture flux from roughly 2200 to 2750 Å, hence the gap in the spectra.

Figures 3, 4, and 5 show the results of our fits to the age, rotation period, and Rossby number evolution of UV emission line fluxes. The emission line fluxes driving these fits, computed from our double-Voigt profiles, are given in Table 4. Table 5 gives the parameters of the fits to emission evolution. In addition to the fits shown, we computed fits excluding the possible K stars in the Tuc-Hor sample. The changes this produced were below the 1σ uncertainties in the fit parameters, generally increasing power law indices by a few hundredths to a tenth and slightly increasing the σ hyperparameter.

6. DISCUSSION

The UV emission of early M stars shows a clear evolution with age and rotation (Figure 2). This is true of both strong emission lines as well as the regions between lines, a pseudocontinuum of weak or unresolved lines and atomic and molecular bound-free opacities (Peacock et al. 2019). For most lines, emission declines by around two orders of magnitude from youth, when emission levels are saturated, to several Gyr. The spectrally resolved evolution we measured refines and extends previously

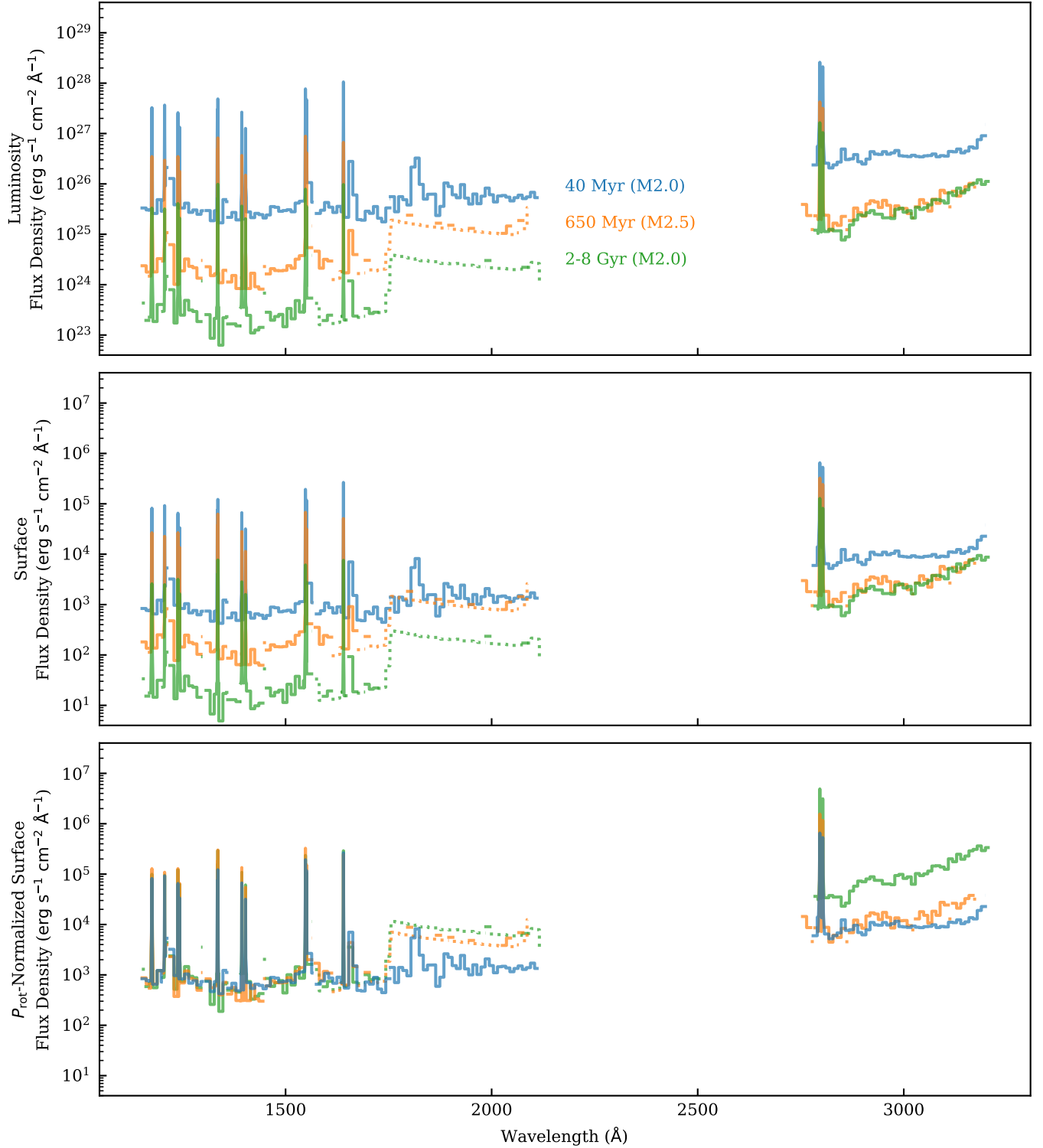


Figure 2. Spectra of representative stars from the stellar sample. The spectra of these fall roughly in the middle of the range of surface fluxes for each group. Strong emission lines have been replaced with their fits and the regions between binned to 10 \AA for higher S/N (see text for more details). Dotted portions of the spectra represent 2σ upper limits where S/N was < 2 . The evolution of the UV luminosities (top panel) and surface fluxes (middle panel) with age over roughly two orders of magnitude is clear. Normalizing by rotation period (bottom panel) results in close consistency between the spectra blueward of 1700 \AA . See the text for further discussion, including of the disparities in the NUV continuum redward of 2700 \AA .

Table 4. UV Emission line surface fluxes in $10^4 \text{ erg s}^{-1} \text{ cm}^{-2}$.

Star	Mg II	C II	Si III	C III	Si IV	He II	C IV	N V	Pseudocont. ^a
J03315	$83.6^{+2.8}_{-0.8}$	$9.1^{+0.9}_{-1.0}$	$3.68^{+0.17}_{-0.09}$	$7.79^{+0.47}_{-0.25}$	$4.10^{+0.10}_{-0.12}$	$13.31^{+0.19}_{-0.34}$	$16.59^{+0.39}_{-0.30}$	$4.9^{+1.0}_{-0.4}$	26.74 ± 0.23
J00240	$87.3^{+1.9}_{-2.3}$	$12.60^{+0.18}_{-0.25}$	$5.93^{+0.11}_{-0.09}$	$9.45^{+0.18}_{-0.23}$	$6.53^{+0.18}_{-0.23}$	$12.86^{+0.27}_{-0.21}$	$18.36^{+0.30}_{-0.33}$	$4.130^{+0.083}_{-0.087}$	26.15 ± 0.73
J02543	$51.0^{+1.9}_{-2.2}$	$5.39^{+0.11}_{-0.25}$	$2.39^{+0.44}_{-0.15}$	$4.73^{+0.31}_{-0.25}$	$3.53^{+0.22}_{-0.31}$	$7.16^{+0.6}_{-0.17}$	$12.3^{+0.6}_{-2.0}$	$3.00^{+0.34}_{-0.44}$	15.95 ± 0.71
J23261	$167.7^{+3.1}_{-3.0}$	$11.67^{+0.33}_{-0.39}$	$4.50^{+0.16}_{-0.13}$	$8.39^{+0.43}_{-0.36}$	$4.82^{+0.17}_{-0.15}$	$15.94^{+0.29}_{-0.23}$	$20.51^{+0.20}_{-0.17}$	$3.63^{+0.14}_{-0.12}$	29.3 ± 1.0
J01521	$34.3^{+1.5}_{-1.7}$	$6.0^{+1.5}_{-1.5}$	$2.12^{+0.46}_{-0.19}$	$6.8^{+1.3}_{-0.4}$	$3.17^{+0.56}_{-0.17}$	$9.93^{+0.80}_{-0.52}$	$9.89^{+0.29}_{-0.28}$	$2.40^{+0.26}_{-0.18}$	15.17 ± 0.79
J00393	$62.8^{+1.6}_{-1.5}$	$7.25^{+0.57}_{-0.22}$	$3.71^{+0.20}_{-0.26}$	$6.84^{+0.65}_{-0.29}$	$4.06^{+0.13}_{-0.13}$	$10.13^{+0.29}_{-0.13}$	$16.34^{+0.57}_{-0.24}$	$3.96^{+0.16}_{-0.27}$	21.21 ± 0.80
J02001	77.2 ± 1.6	$9.69^{+0.28}_{-0.31}$	$3.85^{+0.26}_{-0.14}$	$7.71^{+0.49}_{-0.32}$	$4.38^{+0.87}_{-0.21}$	$15.56^{+0.29}_{-0.28}$	$26.6^{+1.1}_{-0.6}$	$4.56^{+0.34}_{-0.22}$	33.03 ± 0.98
J02365	$146.8^{+1.6}_{-2.4}$	$11.05^{+0.34}_{-0.11}$	$4.182^{+0.037}_{-0.039}$	$6.49^{+0.24}_{-0.17}$	$5.32^{+0.12}_{-0.24}$	$13.94^{+0.15}_{-0.16}$	$16.85^{+0.32}_{-0.27}$	$3.889^{+0.089}_{-0.098}$	25.88 ± 0.20
J22025 ^b	$107.2^{+4.0}_{-4.8}$	16.48 ± 0.24	$10.47^{+0.19}_{-0.22}$	$17.33^{+0.41}_{-0.45}$	$14.70^{+0.26}_{-0.25}$	$11.30^{+0.23}_{-0.39}$	$17.44^{+0.13}_{-0.26}$	5.89 ± 0.16	28.63 ± 0.98
J23285	$150.8^{+3.2}_{-3.2}$	$11.16^{+0.55}_{-0.37}$	3.87 ± 0.13	$9.13^{+0.48}_{-0.89}$	$5.3^{+2.0}_{-0.3}$	$17.33^{+0.25}_{-0.20}$	$16.75^{+0.20}_{-0.23}$	$4.61^{+0.20}_{-0.24}$	31.1 ± 1.1
J22463	77^{+14}_{-14}	$10.24^{+0.37}_{-0.42}$	$3.09^{+0.78}_{-0.18}$	$5.95^{+0.69}_{-0.42}$	$4.49^{+0.22}_{-0.31}$	$9.67^{+0.12}_{-0.17}$	$12.7^{+2.2}_{-0.5}$	$3.92^{+0.41}_{-0.30}$	21.4 ± 1.1
J02125	...	$8.66^{+0.17}_{-0.14}$	$3.83^{+0.09}_{-0.19}$	$5.37^{+0.23}_{-0.15}$	$4.97^{+0.34}_{-0.89}$	$18.0^{+3.6}_{-6.4}$	$15.70^{+0.28}_{-0.24}$	$3.14^{+0.67}_{-0.18}$	24.2 ± 1.3
HAN 192	58.3 ± 1.3	$1.786^{+0.044}_{-0.056}$	$0.556^{+0.052}_{-0.025}$	$1.12^{+0.09}_{-0.17}$	$0.76^{+0.16}_{-0.12}$	$1.77^{+0.11}_{-0.08}$	$2.91^{+0.10}_{-0.09}$	$0.87^{+0.04}_{-0.11}$	3.87 ± 0.28
TYC 1265	$59.3^{+1.8}_{-1.9}$	$1.900^{+0.044}_{-0.052}$	$0.62^{+0.04}_{-0.10}$	$1.38^{+0.12}_{-0.09}$	$0.82^{+0.10}_{-0.14}$	$2.66^{+0.95}_{-0.44}$	$2.94^{+0.11}_{-0.10}$	$0.84^{+0.18}_{-0.08}$	5.74 ± 0.34
LP 415	$39.90^{+0.68}_{-0.52}$	$1.857^{+0.074}_{-0.030}$	$0.65^{+0.07}_{-0.07}$	1.60 ± 0.12	$0.85^{+0.12}_{-0.09}$	$1.740^{+0.068}_{-0.054}$	$4.57^{+0.28}_{-0.19}$	$0.94^{+0.18}_{-0.08}$	4.38 ± 0.23
LP5-282	$119.4^{+2.3}_{-2.0}$	$11.96^{+0.19}_{-0.27}$	$4.29^{+0.09}_{-0.15}$	$6.8^{+1.1}_{-0.5}$	$3.6^{+1.4}_{-0.4}$	$8.98^{+0.15}_{-0.17}$	$16.4^{+1.2}_{-1.4}$	$5.66^{+0.43}_{-0.30}$	25.48 ± 0.63
REID 176 ^c	$26.09^{+0.27}_{-0.29}$
GJ 3290	$40.61^{+0.74}_{-0.78}$	$1.276^{+0.021}_{-0.020}$	$0.364^{+0.017}_{-0.013}$	0.864 ± 0.044	$0.416^{+0.029}_{-0.021}$	$1.20^{+0.23}_{-0.07}$	$2.20^{+0.50}_{-0.06}$	$0.66^{+0.12}_{-0.05}$	3.99 ± 0.22
GJ 176	$17.63^{+0.11}_{-0.09}$	$0.501^{+0.010}_{-0.008}$	$0.1395^{+0.0034}_{-0.0067}$	0.1925 ± 0.0061	$0.1592^{+0.0028}_{-0.0031}$	$0.5332^{+0.0040}_{-0.0062}$	$0.857^{+0.016}_{-0.024}$	$0.2522^{+0.0047}_{-0.0053}$	1.300 ± 0.039
GJ 436	$6.05^{+0.11}_{-0.13}$	$0.1231^{+0.0024}_{-0.0045}$	$0.05045^{+0.00069}_{-0.00067}$	$0.0572^{+0.0011}_{-0.0010}$	$0.0690^{+0.0019}_{-0.0018}$	$0.1401^{+0.0031}_{-0.0024}$	$0.2566^{+0.0056}_{-0.0057}$	$0.0999^{+0.0015}_{-0.0024}$	0.728 ± 0.029
GJ 832	$6.506^{+0.036}_{-0.047}$	$0.1311^{+0.0010}_{-0.0012}$	$0.0420^{+0.0015}_{-0.0011}$	$0.0471^{+0.0011}_{-0.0008}$	$0.05333^{+0.00088}_{-0.00084}$	$0.1828^{+0.0020}_{-0.0015}$	$0.2129^{+0.0036}_{-0.0031}$	0.0851 ± 0.0010	0.494 ± 0.011
G75-55	33.6 ± 1.4	$0.576^{+0.013}_{-0.018}$	$0.233^{+0.047}_{-0.010}$	$0.429^{+0.039}_{-0.028}$	$0.271^{+0.019}_{-0.007}$	$0.892^{+0.046}_{-0.022}$	$1.04^{+0.21}_{-0.03}$	$0.32^{+0.11}_{-0.06}$	1.85 ± 0.12
LTT 2050	7.91 ± 0.32	$0.1839^{+0.0027}_{-0.0043}$	$0.0785^{+0.0048}_{-0.0078}$	$0.1200^{+0.0095}_{-0.0092}$	$0.0813^{+0.0067}_{-0.0082}$	$0.33^{+0.03}_{-0.10}$	$0.365^{+0.020}_{-0.009}$	$0.134^{+0.010}_{-0.017}$	0.586 ± 0.032
GJ 3997	$6.02^{+0.84}_{-0.43}$	$0.1057^{+0.0071}_{-0.0072}$	$0.035^{+0.021}_{-0.016}$	0.233 ± 0.017	$0.080^{+0.062}_{-0.008}$	$0.268^{+0.035}_{-0.018}$	$0.167^{+0.019}_{-0.016}$	$0.052^{+0.012}_{-0.007}$	2.60 ± 0.11
GJ 667C	6.02 ± 0.12	$0.1098^{+0.0033}_{-0.0034}$	$0.0619^{+0.0053}_{-0.0056}$	$0.0794^{+0.0029}_{-0.0023}$	$0.0892^{+0.0028}_{-0.0026}$	$0.2139^{+0.0043}_{-0.0034}$	$0.3344^{+0.0071}_{-0.0050}$	$0.0762^{+0.0019}_{-0.0020}$	0.997 ± 0.044

^aFUV Pseudocontinuum flux integrated over the ranges given in Table 3.^bLine fluxes affected by a double-peaked morphology not captured by the fits. Possible binary. Excluded from evolution fits.^cFUV lines not observed due to detector flare safety regulations.

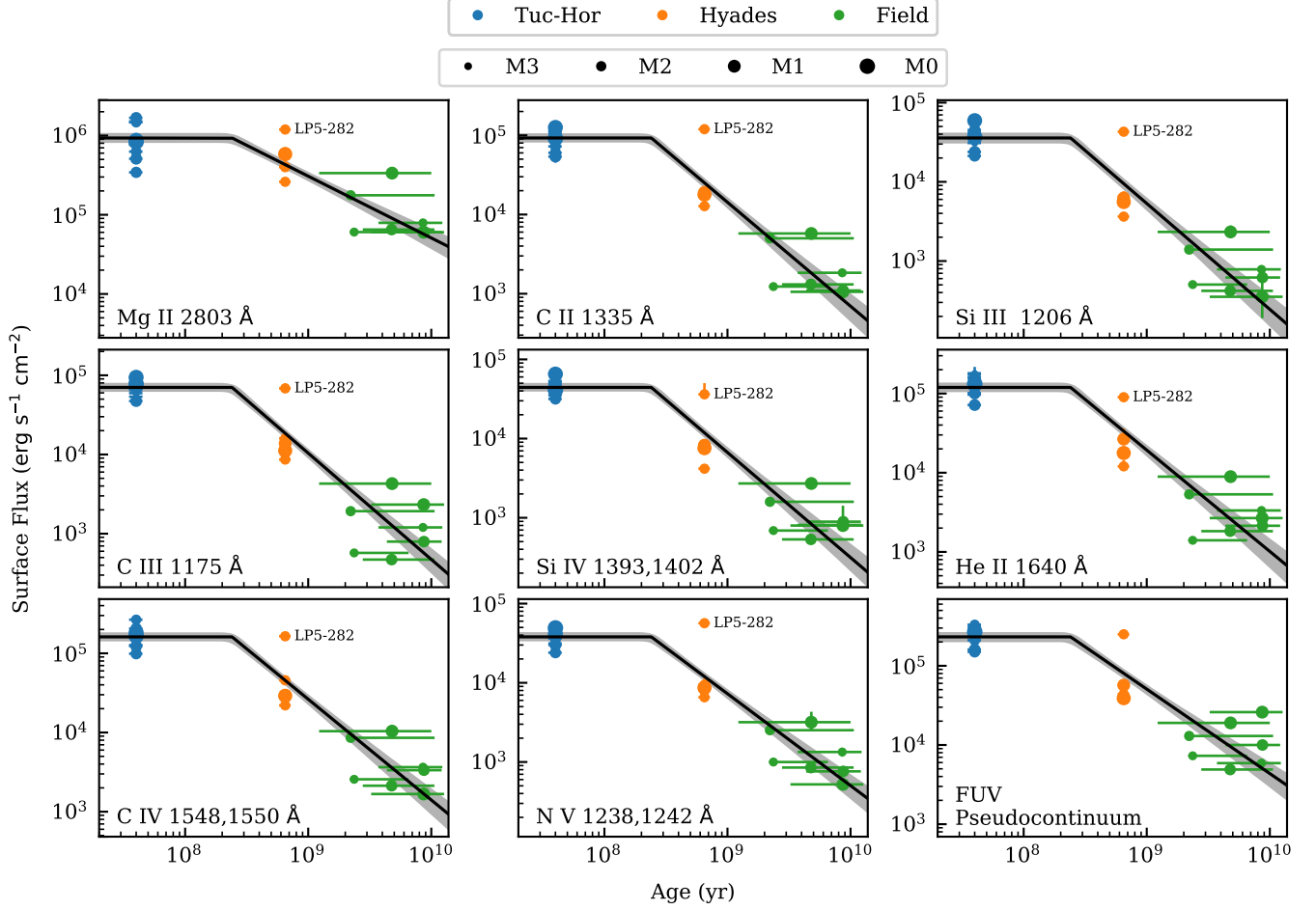


Figure 3. Surface fluxes of strong UV emission lines as a function of age. The component fluxes of multiplets have been added. Error bars are often smaller than the points. Broken power law fits to the evolution of each line are overplotted with gray 68% confidence intervals. The y-axis of each subplot spans the same number of decades to facilitate the comparison of slopes. LP5-282 is highlighted as an outlier in these relationships, but is no longer an outlier in the rotation and Rossby number relationships (Figures 4 and 5).

established relationships between broadband X-ray and UV emission and age (Feigelson et al. 2004; Preibisch & Feigelson 2005; Jackson et al. 2012; Stelzer et al. 2013, 2014; Shkolnik & Barman 2014; McDonald et al. 2019). These spectra will enable improved modeling of the unobservable EUV emission of stars, such as Peacock et al. (2020) carried out using broadband UV measurements.

6.1. Where Emission Forms Influences How It Evolves

Emission sources formed at different regions in the stellar atmosphere exhibit different rates of evolution (Figures 3 - 5). Figure 6 compares the posterior distributions of α from the MCMC evolution fits to each source of emission. As a function of age and rotation, Mg II and FUV pseudocontinuum emission decline less rapidly than most other emission lines. Though ISM absorption is a factor for Mg II, it cannot fully explain this difference (Section 6.2). To quantify the statistical dif-

ference in indices, we determined the fraction of MCMC samples for which the C III decline is as slow or slower than that of Mg II and the FUV pseudocontinuum. For Mg II this occurred in 0.005% of samples (4.1σ) with respect to age and none of 177,000 samples ($> 4.5\sigma$) with respect to rotation period. For the FUV pseudocontinuum, it occurred in 4.6% of samples (2.0σ) with respect to age and 1.3% of samples (2.5σ) with respect to rotation period. This difference in rates of decline causes the ratio of Mg II and FUV pseudocontinuum emission to FUV line emission to evolve by an order of magnitude from young to old ages (Figure 7).

The more gradual evolution of Mg II and (marginally) the FUV pseudocontinuum versus FUV lines must stem from differences in where these lines are formed in the stellar atmosphere. Whereas the FUV lines we analyzed form almost entirely from plasma in the transition region of the stellar atmosphere, Mg II and FUV

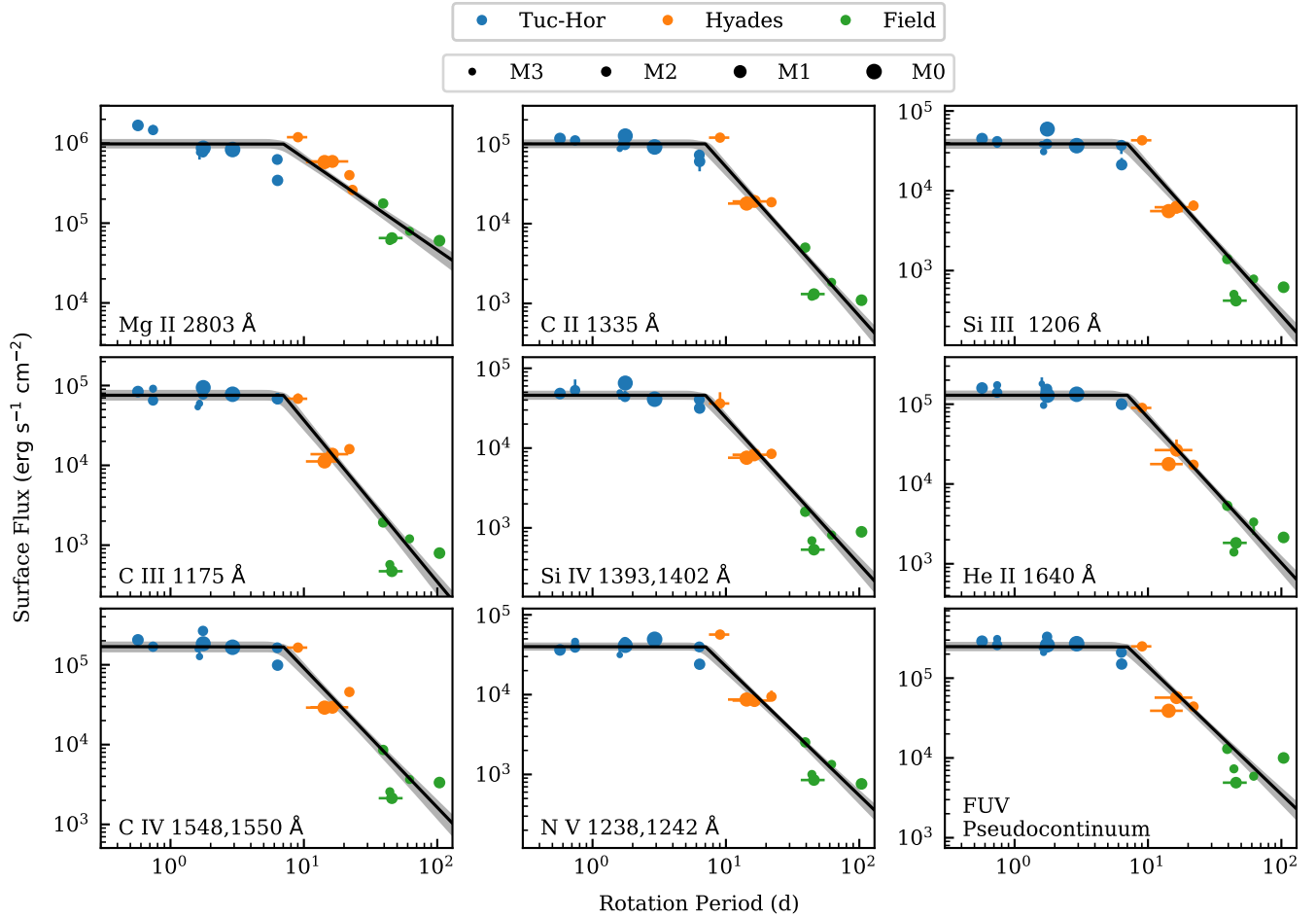


Figure 4. Surface fluxes of strong UV emission lines as a function of rotation period. The component fluxes of multiplets have been added. Error bars are often smaller than the points. Broken power law fits to the evolution of each line are overplotted with gray 68% confidence intervals. The y-axis of each subplot spans the same number of decades to facilitate the comparison of slopes.

pseudocontinuum emission form largely in the stellar chromosphere (Avrett & Loeser 2008; Leenaarts et al. 2013; Linsky et al. 2012). This supports evidence from previous studies that emission from cooler regions of activity-heated stellar atmospheres evolves more slowly with age. Guinan et al. (2003) reported such a trend in *Far Ultraviolet Spectroscopic Explorer* observations of solar analogs, with α ranging from 0.88 (C II 1037 Å) to 1.9 (Fe XVIII 975 Å). For early M stars, Shkolnik & Barman (2014) measured $\alpha = 1.36 \pm 0.32$ in *ROSAT* X-ray flux, 0.99 ± 0.19 in *GALEX* FUV flux, and 0.84 ± 0.09 in *GALEX* NUV flux. The *GALEX* FUV band’s coverage of roughly 450 Å of the FUV pseudocontinuum, while including only three strong emission lines (Si IV, C IV, and He II), could explain why its decline as measured by Shkolnik & Barman (2014) so closely matches that of the FUV pseudocontinuum we measured. EUV fluxes predicted from modeling by Peacock et al. (2020)

of early M star upper atmospheres matched to *GALEX* fluxes yield an age-decline of $\alpha = 1.0$.

The difference in the evolution of Mg II, the FUV pseudocontinuum, and FUV lines could indicate physical differences in the evolution of M star chromospheres and transition regions. Peacock et al. (2020) simulated stellar EUV-NUV emission by modifying PHOENIX models to include a hot upper atmosphere over the star’s photosphere. They defined the temperature structure of the upper atmosphere with three parameters: the depth (in column mass) of the chromospheric temperature minimum, the depth (again, in column mass) at which the transition region begins, and the temperature gradient (versus pressure) of the transition region. While all parameters have an effect across the UV, NUV emission is more sensitive to the depth of the chromospheric temperature minimum than FUV emission. FUV emission is most sensitive to the depth and temperature gradient of the transition region. The change

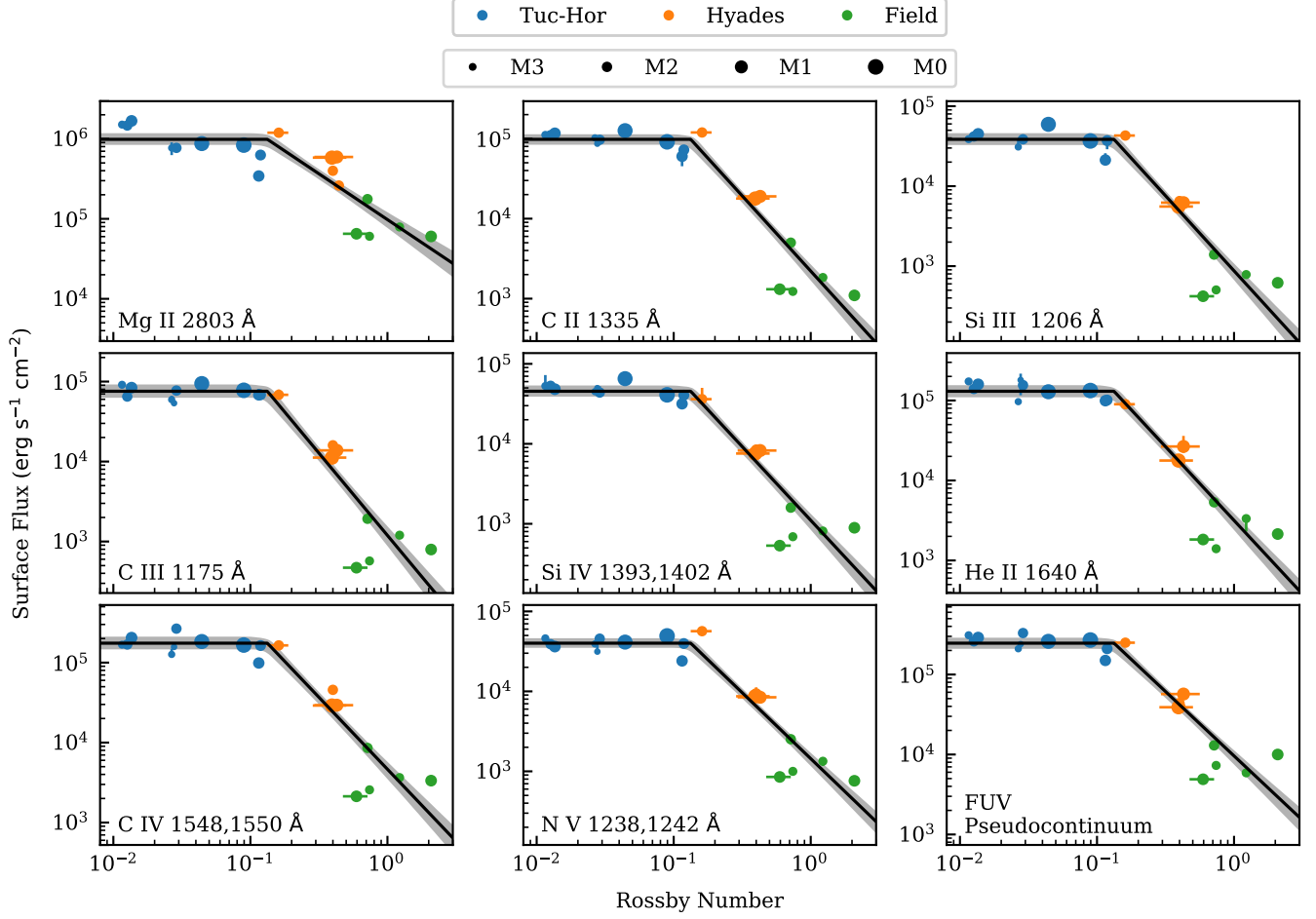


Figure 5. Surface fluxes of strong UV emission lines as a function of Rossby number. The component fluxes of multiplets have been added. Error bars are often smaller than the points. Broken power law fits to the evolution of each line are overplotted with gray 68% confidence intervals. The y-axis of each subplot spans the same number of decades to facilitate the comparison of slopes.

in the Mg II (chromosphere) to FUV line (transition region) flux ratio in Figure 7 during the declining activity phase suggests that the chromospheric temperature minimum is moving upward more slowly than the start of the transition region, though a change in the slope of the transition region temperature gradient could also contribute. In turn, these changes could reflect differences in how the chromosphere and transition region are heated in these stars. If the chromosphere is heated primarily by acoustic shocks launched from photospheric convection rather than magnetic activity (Wedemeyer et al. 2004), it would be less affected than the transition region as M stars age.

Linsky et al. (2020) recently conducted a similar analysis, examining the ratio of X-ray (coronal) to reconstructed Ly α (chromospheric) emission as a function of spectral type and activity level. They found that X-ray emission decreases more rapidly than Ly α emission toward lower activity levels (older ages) for all types, akin

to the more rapid evolution of FUV line versus Mg II emission we observed. For M stars, Linsky et al. (2020) found this discrepancy to be less pronounced, suggesting the differences in line evolution we have observed would grow toward earlier spectral types.

The budget of UV emission changes considerably over the lifetime of an early M star. At around a period of 30 d, between the age of the Hyads and the field stars, the FUV pseudocontinuum begins to account for more FUV flux than strong FUV lines, excluding the Ly α line, which dominates at all ages (Figure 7). Assuming the empirical $F_{\text{Ly}\alpha} = 60F_{\text{Mg II}}^{0.77}$ relationship of Youngblood et al. (2016) is constant with age and rotation, Ly α would evolve as $t^{-0.6}$, $P_{\text{rot}}^{-0.9}$, and $Ro^{-0.9}$ (though see Section 6.2). Its emission exceeds combined FUV line and pseudocontinuum emission by a factor of 5-7 during saturation, increasing to 40-80 by 10 Gyr. These changes in the UV energy budget with age will affect

Table 5. Fits of emission line surface flux evolution with age, rotation, and Rossby number.

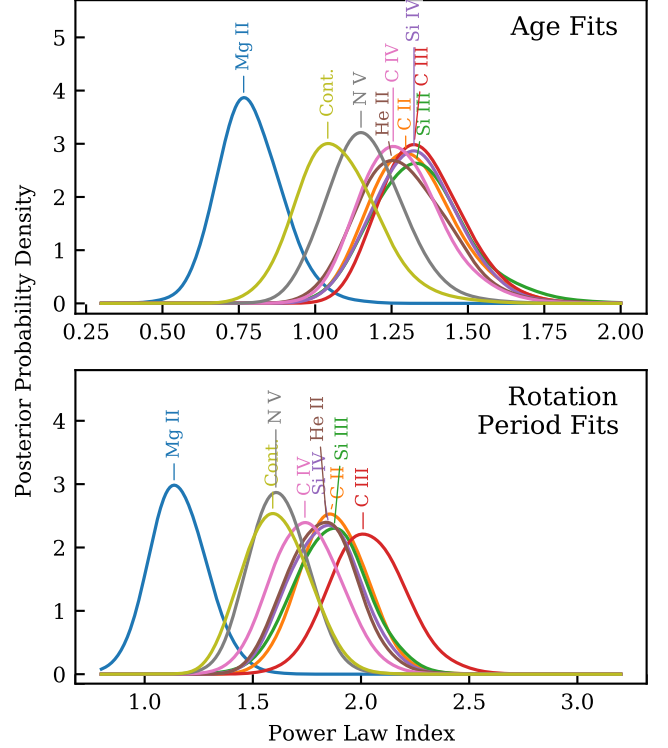
Line	$\log_{10}(F_{\text{sat}})$ erg s ⁻¹ cm ⁻²	α	σ	$\hat{\sigma}_{\text{TH}}$	$\hat{\sigma}_{\text{Hy}}$	$\hat{\sigma}_{\text{Fld}}$
Age						
$\log_{10}(x_{\text{sat}}/\text{yr}) = 8.381^{+0.046}_{-0.050}$						
Mg II	$5.970^{+0.064}_{-0.063}$	$0.78^{+0.11}_{-0.09}$	0.21	0.21	0.20	0.28
C II	$4.967^{+0.060}_{-0.059}$	$1.31^{+0.14}_{-0.12}$	0.21	0.11	0.35	0.32
Si III	$4.554^{+0.068}_{-0.071}$	$1.34^{+0.15}_{-0.14}$	0.23	0.12	0.37	0.35
C III	$4.847^{+0.058}_{-0.056}$	$1.34^{+0.14}_{-0.12}$	0.19	0.09	0.31	0.48
Si IV	$4.646^{+0.057}_{-0.053}$	$1.33^{+0.14}_{-0.13}$	0.19	0.08	0.31	0.35
He II	$5.077^{+0.061}_{-0.060}$	$1.28^{+0.16}_{-0.13}$	0.21	0.12	0.30	0.39
C IV	$5.208^{+0.058}_{-0.057}$	$1.27^{+0.14}_{-0.12}$	0.20	0.11	0.31	0.33
N V	$4.580^{+0.060}_{-0.057}$	$1.16^{+0.13}_{-0.11}$	0.19	0.09	0.34	0.27
Cont. ^a	$5.365^{+0.061}_{-0.067}$	$1.07^{+0.14}_{-0.11}$	0.21	0.11	0.31	0.38
Rotation Period						
$\log_{10}(x_{\text{sat}}/\text{d}) = 0.846^{+0.040}_{-0.085}$						
Mg II	$5.993^{+0.062}_{-0.058}$	$1.15^{+0.13}_{-0.12}$	0.19	0.20	0.07	0.18
C II	$5.000^{+0.056}_{-0.055}$	$1.87^{+0.15}_{-0.14}$	0.17	0.09	0.18	0.26
Si III	$4.588^{+0.064}_{-0.062}$	1.86 ± 0.16	0.19	0.11	0.20	0.31
C III	$4.878^{+0.069}_{-0.068}$	$2.03^{+0.17}_{-0.16}$	0.22	0.08	0.20	0.36
Si IV	$4.662^{+0.057}_{-0.058}$	$1.84^{+0.15}_{-0.16}$	0.18	0.08	0.15	0.31
He II	$5.112^{+0.060}_{-0.063}$	$1.82^{+0.15}_{-0.16}$	0.19	0.10	0.14	0.32
C IV	$5.227^{+0.065}_{-0.071}$	$1.75^{+0.16}_{-0.15}$	0.21	0.11	0.21	0.30
N V	$4.601^{+0.052}_{-0.050}$	1.62 ± 0.13	0.15	0.09	0.20	0.21
Cont. ^a	$5.395^{+0.059}_{-0.056}$	$1.60^{+0.15}_{-0.14}$	0.18	0.09	0.18	0.30
Rossby Number						
$\log_{10}(x_{\text{sat}}) = -0.876^{+0.037}_{-0.061}$						
Mg II	$5.994^{+0.077}_{-0.070}$	1.15 ± 0.16	0.23	0.20	0.12	0.24
C II	$4.992^{+0.065}_{-0.068}$	1.88 ± 0.16	0.22	0.09	0.04	0.37
Si III	$4.586^{+0.077}_{-0.073}$	$1.88^{+0.18}_{-0.17}$	0.23	0.11	0.06	0.42
C III	$4.879^{+0.085}_{-0.083}$	2.06 ± 0.20	0.27	0.08	0.09	0.49
Si IV	$4.657^{+0.073}_{-0.067}$	$1.84^{+0.17}_{-0.15}$	0.22	0.08	0.05	0.42
He II	5.116 ± 0.075	$1.84^{+0.16}_{-0.15}$	0.23	0.10	0.11	0.42
C IV	$5.243^{+0.081}_{-0.077}$	1.80 ± 0.17	0.25	0.11	0.08	0.42
N V	$4.603^{+0.062}_{-0.059}$	1.65 ± 0.14	0.19	0.09	0.06	0.32
Cont. ^a	$5.392^{+0.068}_{-0.070}$	$1.61^{+0.16}_{-0.15}$	0.22	0.09	0.09	0.39

^aFUV pseudocontinuum.

NOTE—Fits follow the form

$$F = \begin{cases} F_{\text{sat}}, & x \leq x_{\text{sat}} \\ F_{\text{sat}} (x/x_{\text{sat}})^{-\alpha}, & x > x_{\text{sat}} \end{cases} \quad (2)$$

where F is surface flux, x is a placeholder for age [yr], rotation period [d], or Rossby number [dimensionless], and sat stands for saturation. All lines share the same x_{sat} and were fit simultaneously. The intrinsic scatter, σ , was included as a hyperparameter to the fit. The sample standard deviation of points about the median fit, $\hat{\sigma}$, is also included for the Tuc-Hor (TH), Hyades (Hy), and Field (Fld) groups separately.

**Figure 6.** Smoothed posterior distributions for the index of the power law decline in quiescent activity for strong UV emission lines. Most are statistically indistinguishable. However, Mg II shows a significantly less rapid decline (lower index) relative to C III and most other FUV lines, likely because a fraction of Mg II emission originates from radiative excitation of ions in the stellar photosphere rather than the activity-heated upper atmosphere.

the balance of molecular photolysis in the upper atmospheres of orbiting planets.

6.2. ISM Absorption of Mg II

The more gradual evolution of Mg II flux begs the question of whether ISM absorption could be at play. Because the younger stars of the sample are further away, the column density of Mg^+ ions in the line of sight will likely be larger for them. This could suppress the Mg II flux of those stars, artificially shrinking the difference between the Mg II flux of the young (far away) and old (nearby) stars (i.e., lowering α).

ISM absorption is likely affecting the Mg II fluxes we measured. For cool, main sequence stars at distances representative of the Tuc-hor objects (35-50 pc), Redfield & Linsky (2002) measured Mg II column depths between $10^{12.34}$ and $10^{13.14}$ cm⁻² and Doppler broadenings of 2.1 to 4.3 km s⁻¹. For a star with an intrinsically narrow Mg II line such as that of GJ 832 (FWHM 18 km s⁻¹; France et al. 2013), these ranges correspond to absorption varying from 17-53%. Broader Mg II lines

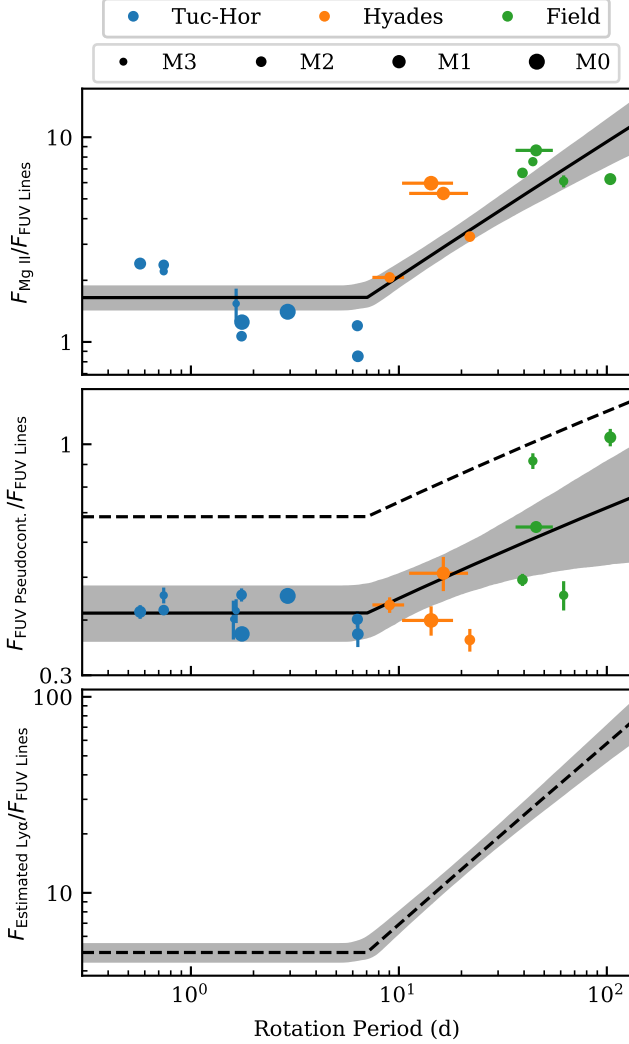


Figure 7. Evolution of UV flux ratios as early M stars spin down. The slower evolution of Mg II and pseudocontinuum flux corresponds to an increase in these ratios with rotation. “FUV lines” refers to every strong line (i.e., commensurate with Si IV) in the 1160-1740 Å range except O I and Al II. Including these would increase the summed FUV line flux by $\sim 10\%$. Mg II observations (with the G230L grating) were usually contemporaneous to within a day of those of FUV lines (with the G130M and G160M gratings), though in some instances the two were separated by years. The dashed line in the middle panel scales the FUV pseudocontinuum flux integration to fill gaps in its 1160-1740 Å range. See text for details on Ly α estimation. The flux of Mg II and Ly α exceeds FUV lines at all ages, whereas the FUV pseudocontinuum transitions from contributing less to more flux than FUV lines at a period of around 30 d, between Hyades and field ages.

will have more flux shifted outside of the narrow ISM absorption, lessening this affect. Of the young stars in the sample, the FWHMs of our Mg II fits for 11 of 18 stars are greater than 50 km s^{-1} , well above the 30 km s^{-1} LSF of the G230L grating. For the broadest of these, ISM absorption could fall below 1%.

This range of possible ISM absorption is too small to explain the more gradual evolution of Mg II emission with age. However, it could contribute to the scatter of Mg II emission (Figure 4) and its apparent evolution with rotation period even during saturation for the Tuc-Hor objects (Figures 4 and 7). The Tuc-Hor objects span an order of magnitude in rotation period, with rotational speeds fast enough to significantly broaden their emission lines. The broader lines of faster rotating stars will be less affected by the narrow ISM absorption, potentially producing the observed trend. However, statistically this trend is marginal, with a p -value of 0.005 (2.6σ) that weakens to 0.02 (1.7σ) when considering each panel of Figure 4 as a separate trial of the null hypothesis.

If ISM absorption is impacting the observed flux of the slowest rotating Tuc-Hor objects, then the Mg II emission of the fastest rotating objects could be a better estimate of the Mg II saturation level. Accordingly, the rates of Mg II decline with age, rotation, and Rossby number should be regarded as lower limits, with the true α values possibly up to 0.2 higher.

6.3. Predicting the UV Emission of M Stars, Present, Past, and Future

This work adds to a growing list of resources readers could use to estimate the UV emission of early M stars. Such resources are invaluable given that *HST*’s eventual end of life is likely to leave a long gap in UV observational capabilities. For convenience, Table 6 outlines and compares the resources presently available.

6.3.1. UV Line Fluxes

The relationships we derived enable the emission from strong UV lines and the FUV pseudocontinuum to be estimated from age or rotation period with a 1σ precision of 0.2 dex, less than a factor of 2. There is greater scatter in the fits to Rossby number than age or rotation period, with a typical precision of 0.2-0.3 dex. For a sample of stars diverse in spectral type, casting quiescent activity evolution in terms of Rossby number should, by design, increase the consistency of points around a saturation-decay model by accounting for differences in the strength of convection. In this case, however, the sample spans a narrow range in spectral type, and it appears that attempting to infer convective turnover rates in an effort to improve quiescent activity evolution fits only introduces

noise, perhaps due to metallicity differences in the field sample in particular (Table 1). We include the Rossby number fits due to their long heritage in the literature and because they could be of use in estimating UV fluxes for a star outside of the M0 to M2.5 range. However, because our fits exclude any such stars, doing so would essentially be an extrapolation and should accordingly be done with caution. The UV line flux measurements versus rotation period plots of [France et al. \(2018\)](#) provide a useful point of comparison for a broad range of spectral types.

The precision with which rotation period and age predict stellar FUV line emission for early M stars exceeds that of optical activity indicators. Recently [Melbourne et al. \(2020\)](#) assembled a sample of nearly 70 stars spanning M0 to M9 types and computed empirical fits of UV line fluxes versus Ca II *S*-index, Ca II R'_{HK} , and $L_{H\alpha}/L_{bol}$ for the sample, updating earlier work by [Youngblood et al. \(2017\)](#). Scatter about their power-law fits between Ca II R'_{HK} and UV lines range from 0.4-0.6 dex, with the exception of Mg II at 0.31 dex. Their sample included all HAZMAT targets and covered ages ranging from 10 Myr to 10 Gyr. The larger scatter in these UV-optical relationships versus the UV age and rotation relationships we derived could come from a number of sources. Chief among these are the larger range of spectral subtypes and the gaps in time between the optical and UV activity observations. Flares, though sometimes present, likely do not contribute significantly ([Melbourne et al. 2020](#)). Differences in the formation region of Ca II H & K emission versus strong FUV lines could be a factor, since Ca II H & K emission forms primarily in the stellar chromosphere ([Björger et al. 2018](#)). This is supported by the lower level of scatter in fits between Ca II H & K and Mg II than Ca II H & K and FUV lines.

6.3.2. *Scaling Spectra*

The entire FUV spectrum (with the exception of Ly α) of an early M star can be predicted reasonably well by simply scaling the FUV spectrum of a template star along a saturation-decline track. The bottom panel of Figure 2 illustrates this, wherein all spectra have been scaled to match a rotation period of 10 d via a saturation-decline track with $t_{sat} = 10$ d and $\alpha = 2$. This brought the spectra into good alignment with each other, differing in both the line and continuum regions generally by less than a factor of a few for the FUV.

The NUV regions of the spectra in Figure 2 (the data spanning 2750-3250 Å) show a markedly different trend than the FUV. NUV pseudocontinuum emission at 650 Myr and Gyr ages is almost identical, but at

40 Myr it is elevated by an order of magnitude. Meanwhile, FUV pseudocontinuum emission differs by an order of magnitude between each age group. The reason for this is simply the differing contribution of emission from the stellar photosphere, which shows comparatively little evolution with age. For field-age stars, NUV pseudocontinuum emission is dominated by the stellar photosphere (e.g., [Lloyd et al. 2016](#), Figure 12). For 40 Myr stars, activity-generated emission dominates, elevating the NUV pseudocontinuum, but by 650 Myr activity-generated emission has already fallen below photospheric levels. A similar result is evident in the analysis of [Shkolnik & Barman \(2014\)](#). Their work showed that the fraction of emission attributable to early M star photospheres in the *GALEX* NUV bandpass, while minimal at young ages, can reach 40% by Gyr ages. The *GALEX* NUV band (predominantly 1800-2750 Å) lies blueward of the region under consideration here (2750-3250 Å), so it is not surprising that photospheric emission dominates as early as 650 Myr onward in the present case. This fact is what causes the NUV portions of the spectra in the lower panel of Figure 2 to reverse order from the top panel.

6.3.3. *Caveats and Areas for Improvement in Predicting UV Emission*

The ages of the field stars are very uncertain, influencing the fits. Incorporating these uncertainties into the evolution fits described in Section 4.2 increased uncertainty in the rate of activity decline by up to 50% and allowed the fits to better accommodate the Hyades data. However, the fits assumed these estimates and associated uncertainties are independent. In reality, the ages could be systematically high or low if the isochrones or gyrochrones used in the age determination are inaccurate (see, e.g., [Angus et al. 2020](#) for an investigation of systematic errors in M star gyrochrones). The possibility of a systematic offset means that the uncertainty in the fits to activity evolution with age should be taken as a lower limit. A systematic shift of ages to higher or lower values in log space would correspond to a roughly equivalent change in the value for the index of the power law decline, α . We expect any systematic offset in the ages of the field stars to be no more than a factor of two (0.3 dex), implying any additional uncertainty in α for the ages fits of Table 5 will be under 0.3. Since this would affect all lines equally, it does not affect our conclusions regarding differences in evolution between emission sources.

The differences between the model and photometric radii of young stars is a factor in predicting their UV luminosity. The 10-60% differences between these two radii correspond to a factor of 1.2-2.6 in surface flux.

Table 6. Options for predicting the FUVUV emission of early M stars.

Stellar Type	Data Available	Emission Source of Interest	Recommended Procedure	Accuracy, Limitations, and Caveats
1 M0 - M2.5	rotation period or age	C III, Si III, N V, C II, Si IV, C IV, He II, Mg II or unresolved FUV pseudo-continuum	scale using relationships in Table 5	< a factor of 2
2 M1 and M2	rotation period or age	full UV spectrum, resolved continuum and EUV	pick closest match from Peacock et al. (2020), scale by P_{rot}^{-2} or $t^{-1.3}$	factor 1-10 in major FUV lines, more accurate in broadband flux (see Peacock et al. 2019), some strong spurious lines can be identified and masked by comparison to a spectrum from this work or Loyd et al. (2016), does not include coronal EUV emission sources (a minimal contributor to total EUV flux), consider photosphere when scaling above 2000 Å (Section 6.3)
3 K1 - M5	rotation period or age	full UV spectrum, unresolved continuum and EUV	pick closest match from Loyd et al. (2016) (reference also France et al. 2016; Youngblood et al. 2016), scale by P_{rot}^{-2} or $t^{-1.3}$	factor of 2-4 in major FUV lines and broad continuum, O I 1305 Å lines masked due to telluric contamination, no data below roughly 1150 Å, consider photosphere when scaling above 2000 Å (Section 6.3)
4 M0 - M9	Ca II <i>S</i> index, Ca II R'_{HK} , or $L_{H\alpha}/L_{\text{bol}}$	Si III, Ly α N V, Si II, C II, Si IV, C IV, He II, Mg II	Melbourne et al. (2020)	factor of 2-4 if using <i>S</i> or R'_{HK} or 2.5-5 if using $L_{H\alpha}/L_{\text{bol}}$
5 K-M	Mg II, Si III, or C IV flux	Ly α	Youngblood et al. (2016)	generally 10%, unknown Ly α self-absorption could introduce factor 2 inaccuracy
6 M1 and M2 or K1-M5	<i>GALEX</i> FUV or NUV or other UV emission measurement	full UV spectrum	see (2) or (3), subtract photosphere, scale remainder to match measured flux, add photosphere	see (3), beware that scaling by a single emission line could yield corresponding inaccuracy in broadband FUV flux, consider photosphere when scaling above 2000 Å (Section 6.3)
7 M0 - M2.5	None	evolution of C III, Si III, N V, C II, Si IV, C IV, He II, Mg II or unresolved FUV pseudocontinuum	see (1)	< a factor of 2 for the population average; however, saturation lifetime could vary by more than an order of magnitude for individual stars (Tu et al. 2015) and the rate of spin-down and associated activity decline is not likely to be constant (Section 6.3)
8 M1 and M2	None	evolution of full UV spectrum, resolved continuum and EUV	interpolate from age grid of Peacock et al. (2020)	factor 1-10 in major FUV lines, more accurate in broadband flux, see also (2) and (8)

This means that scaling a surface flux from this work to the model radius of a pre-main-sequence star could yield an underestimate of the star’s UV luminosity.

An important factor in fitting the quiescent activity evolution of a sample of stars is that this fit will represent a population average. In reality, each star will follow its own track, equivalent to an ensemble of lines instead of a single line in Figure 3. The primary difference in this ensemble of tracks would be the lifetime of saturation. As a result, the scatter in quiescent activity levels for a group of coeval stars will grow as stars in that group progressively transition from saturated to declining activity.

Evidence is mounting that the spin down rate of M stars varies with time. The spin down of K through early M stars appears to stall around the age of the Hyades, with the spin down of lower-mass objects stalling for a longer period of time (Agüeros et al. 2018; Curtis et al. 2019; Douglas et al. 2019). Early M stars in the *Kepler* field make up two distinct populations of rotators, with the modal rotation period of one population at 19 d and the other at 33 d (McQuillan et al. 2013). This could be a result of episodic star formation, as McQuillan et al. (2013) infer, or stalled spin down around 19 d. At lower masses, Newton et al. (2016, 2018) found a wide range of rotation periods, 10-70 d, that are poorly represented

among the population of nearby mid M stars and concluded that this is the result of periods of slowed and accelerated spin down.

Modeling by Spada & Lanzafame (2020) that incorporates rotational coupling between the radiative and convective zones of stars yields variable spin-down rates and shows promise in reproducing the age-rotation demographics of low-mass stars (Angus et al. 2020). Coupling a spin-down model like that of Spada & Lanzafame (2020) to activity-rotation relationships like those presented here can yield a model where each star follows its own track based on its initial rotation rate, and where these tracks do not decline linearly in log space but instead reflect variable spin down rates. Johnstone et al. (2020) recently created a coupled activity-spin-down model for the purposes of predicting the combined EUV and X-ray (together, XUV) evolution of stars that powers mass loss from orbiting planets. Future work could do the same for FUV emission to enable better modeling of photochemistry in planetary atmospheres as stars evolve. As data on M star rotational evolution improves, coupled age-rotation-activity models will become increasingly accurate.

6.4. *What are the sources of scatter in these relationships?*

The scatter in the quiescent activity of stars of the same age in this sample is intrinsic to the star. Measurement uncertainties are well below the 0.2-0.3 dex scatter. The absolute flux calibration of COS is accurate to roughly 5% (0.02 dex; Dashtamirova et al. 2020). Two other potential sources of scatter are immediately dismissable. Flares cannot be a significant contributor to the scatter because these data are time resolved, which enabled us to clean the spectra of detectable flares (Lloyd et al. 2018b). Note, however, that flares are an important, possibly dominant, source of both line and continuum UV emission in M stars (Lloyd et al. 2018a,b). Differences in spectral subtypes cannot be the source of scatter because there is no clear ordering by subtype (point size in Figures 3, 4, and 5) in whether line fluxes lie above or below the evolution trend line.

Eliminating the above sources of scatter leaves metallicity differences, scatter in seed rotation rates, age uncertainty, long-term activity cycles, and rotational variability as possible sources of the observed scatter in quiescent stellar activity. For the Tuc-Hor sample, metallicity, seed rotation rates, and age uncertainty cannot contribute to the observed scatter. Differences in their seed rotation rates cannot contribute because the stars are all in the saturated activity regime, where rotation rate does not influence quiescent activity. They are un-

likely to have substantial differences in metallicity or age because they formed from the same cloud (Taberner et al. 2012). Hence, the scatter of the Tuc-Hor sample can only be due to long-term activity cycles or rotational variability. These two effects, combined, must account for the roughly 0.1 dex (25%) scatter in the fluxes of the FUV emission lines from these stars. This is supported by a recent analysis of X-ray emission from stellar populations by Johnstone et al. (2020) that controlled for various sources of scatter and found activity cycles to be the dominant contributor, though the scatter they analyzed was at the level of 0.36 dex.

The only difference between the Tuc-Hor and Hyades groups that could influence differences in their scatter is variability in their seed rotation rates. Because the Hyades stars are (mostly) no longer in the saturated activity regime, differences in their seed rotation will affect their activity evolution by setting the point at which the star will transition from saturated to declining activity. For Sun-like stars, differences in seed rotation can drive differences in the duration of their saturated activity spanning over an order of magnitude (Tu et al. 2015). The present sample reflects this effect, with scatter growing from 0.1 dex at the age of Tuc-Hor to > 0.3 dex (> 100%) at the age of the Hyades. LP5-282 drives this scatter; however, it is not a rotational outlier when compared to a larger group of early M Hyads (Douglas et al. 2019). Within the present sample, LP5-282 likely formed with the highest seed rotation rate, delaying its transition out of saturated activity and shifting its evolutionary track as a function of age to the right by about a factor of two in Figure 3.

For the field sample, differences in metallicity and age uncertainty are added as possible contributors to scatter. This likely explains why this group has the largest scatter of the three.

6.5. *Does the First 100 Myr of Emission Matter Most to Planets?*

Recently, King & Wheatley (2020) challenged the widespread conclusion that the first 100 Myr of a star’s XUV emission are responsible for the bulk of planetary atmospheric loss (e.g., Lopez & Fortney 2013; Luger et al. 2015; Owen & Wu 2017). There are no direct measurements of the age-evolution of the “soft” (360-912 Å) range of stellar EUV (100-912 Å) evolution because absorption from intervening ISM gas blocks it from observation. King & Wheatley (2020) inferred the evolution of stellar EUV emission by combining observations of the age-evolution of stellar X-ray emission (Jackson et al. 2012) with an empirical trend for the Sun that relates X-ray to EUV luminosity variations (King et al. 2018).

The resulting slope in the power-law decay of EUV emission, α , spans 0.63-0.81 and, for soft EUV emission, 0.26-0.33, for FGK spectral types. For the lowest mass bin of stars, with $B - V$ from 1.275 to 1.41, corresponding to roughly K6 to M0 stars⁵, $\alpha = 0.68 \pm 0.22$ (full EUV) and $0.28_{-0.09}^{+0.20}$ (soft EUV). Such shallow rates of decline would make the EUV emission of a star at Gyr ages more important to planetary atmospheric escape than previously thought.

The actual rate of decline in EUV emission from late K and early M stars, and probably other types as well, is likely to be more rapid than King & Wheatley (2020) suggest. An M star’s EUV emission comes primarily from transition region plasma, albeit with significant contributions from the corona and chromosphere (Fontenla et al. 2016; Peacock et al. 2019). It therefore seems likely that the age-evolution of broadband EUV emission will fall near that of FUV emission from the transition-region, roughly $\alpha = 1.3$, and within the bounds set by the evolution of chromospheric Mg II and coronal X-ray emission, $\alpha = 0.8 - 1.35$ (Shkolnik & Barman 2014). Peacock et al. (2020) derive a value in this range, $\alpha = 1.0$, for the evolution of early M star EUV emission based on stellar atmospheric models anchored by broadband FUV and NUV flux measurements from *GALEX*, excluding coronal EUV emission. In contrast, taking the late-K/early-M bin from King & Wheatley (2020) to be comparable to our sample, the King & Wheatley (2020) values for α imply that EUV emission declines more slowly than emission both redward and blueward of the EUV band for early M stars. We caution, however, that the overlap in the spectral types of these two samples is marginal, intersecting only at M0.

Regardless of the true rate of decline in EUV emission, King & Wheatley (2020)’s conclusion that the majority of XUV radiation is emitted on Gyr timescales holds true. Figure 8 plots the time-integral of emission over the age of the universe for saturation lifetimes spanning an order of magnitude (Tu et al. 2015), centered on our best-fit value of $t_{\text{sat}} = 240$ Myr, and rates of decline ranging between the value we estimate for Ly α , $\alpha = 0.6$, to that we found to be typical of our fits to transition-region FUV line emission, $\alpha = 1.3$. We accounted for changes in stellar radius of a $0.5 M_{\odot}$ star as predicted by the MIST stellar evolution models (Dotter 2016; Choi et al. 2016), though see Section 2. Lifetime-integrated emission varies by a factor of a few between these scenarios. Mathematically, a rate of decline with $\alpha > 1$ implies that the cumulative flux will approach an

asymptote with age, whereas $\alpha < 1$ implies cumulative flux is unbounded.

In most cases, the majority of lifetime-integrated emission occurs after 100 Myr. The exception is the $\alpha = 1.3$ and $t_{\text{sat}} = 76$ Myr case, for which the cumulative emission is roughly evenly divided before and after the 100 Myr mark. For comparison, we also plot the time-integral of the XUV emission tracks adopted by Lopez & Fortney (2013) and Owen & Wu (2013), works that predicted the later observed exoplanet radius valley. These XUV emission tracks are from Ribas et al. (2005) and Jackson et al. (2012) for G stars. Note that they are normalized to their values at 13.8 Gyr for comparison, even though G star planets will, in general, receive less XUV flux over their lifetimes than M star planets with similar equilibrium temperatures.

Although the bulk of XUV emission might occur after 100 Myr, the first 100 Myr or so of a star’s XUV emission could still be the most important to determining a planet’s atmospheric loss. For a planet whose mass is dominated by its core, mass is most easily removed early in life when the atmosphere is in its most distended state, lofting gas higher out of the planet’s gravitational well. As both mass is lost and the atmosphere radiatively cools and contracts, the remaining mass recedes deeper into the planet’s gravitational well. Hence, atmospheric loss would slow with time even if XUV irradiation did not decline at all (e.g., Luger et al. 2015; Owen & Wu 2017). This could be exacerbated by a transition from recombination-limited to energy-limited mass loss (Murray-Clay et al. 2009), causing further drops in XUV irradiation to drive a linear ($\dot{M} \propto F_{\text{XUV}}$) instead of a square root ($\dot{M} \propto F_{\text{XUV}}^{0.5}$) drop in the mass loss rate. We expect that the combination of these considerations will make the first 100 Myr a critical phase of atmospheric loss for a planet, regardless of whether XUV emission declines as $t^{-0.7}$, as King & Wheatley (2020) propose, or at a rate closer to $t^{-1.3}$, as we propose.

7. SUMMARY

We have presented results from *HST* UV spectroscopy of 25 M0-M2.5 stars in three distinct age groups, 40 Myr, 650 Myr, and field ages. For the first time, we resolved the evolution of individual UV emission lines with both age and rotation. Flux from Mg II, an oft-used proxy for Ly α , as well as flux within broad FUV pseudocontinuum bands, declined by 1 and 1.5 orders of magnitude, respectively, whereas strong FUV lines dropped by roughly 2 orders of magnitude. These differences are in line with previous observations showing that emission formed lower in the activity-heated upper atmospheres of stars declines less rapidly with age. In consequence,

⁵ From the table compiled by STScI, <https://www.stsci.edu/~inr/intrins.html>

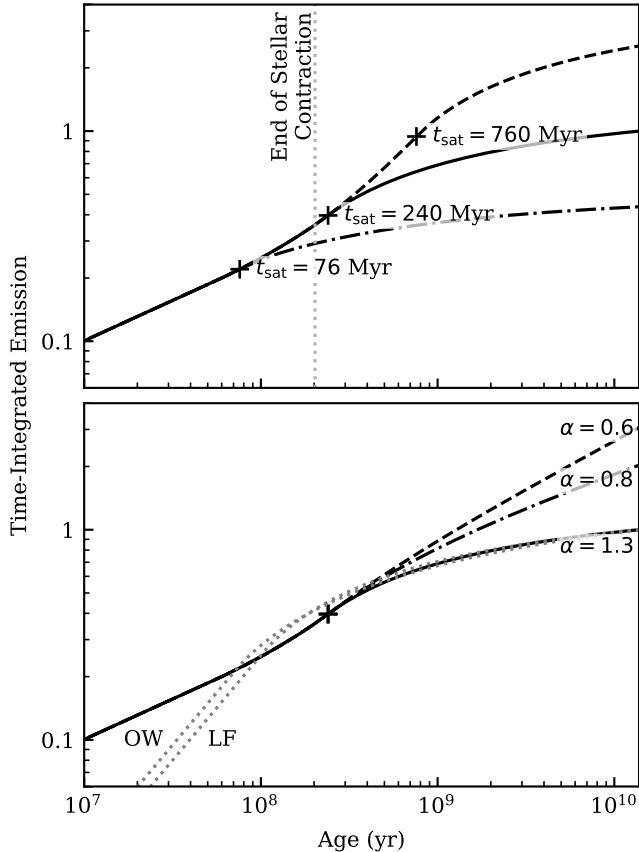


Figure 8. Cumulative emission for a variety of activity evolution scenarios. The upper plot varies the activity saturation lifetime to show the possible effect of different stellar seed rotation rates. The lower plot shows the effect of different indices of the power law decline. A power-law index of $\alpha = 1.3$ is typical of FUV lines and X-ray emission, 0.8 matches Mg II, and 0.6 is a possible value for Ly α (see text). Note that all curves are normalized to the value at 13.8 Gyr for $t_{\text{sat}} = 240$ Myr (our best fit value) and $\alpha = 1.3$. The pre-main-sequence stellar contraction of a $0.5 M_{\odot}$ star is included, ending at the dotted vertical line. These curves likely bracket cumulative EUV emission, though we consider the $\alpha = 1.3$ curve (valid for FUV line emission) as likely to be the best proxy for the EUV. Dotted lines in the lower plot show the models adopted by Lopez & Fortney (2013, LF) and Owen & Wu (2013, OW), normalized to the value at 13.8 Gyr. The majority of energy is emitted after 100 Myr in most cases.

the energy budget of UV flux from early M stars becomes weighted more toward “cooler” sources of emission as early M stars age.

We fit a model of constant saturation followed by a power-law decay to the evolution of each emission line. Equipped with an age or rotation period for an arbitrary early M star, the reader can use fits from Table 5 to predict that star’s quiescent emission in the strong UV lines C II, C III, C IV, He II, Mg II, N V, Si III, and

Si IV and the unresolved FUV pseudocontinuum to a 1σ accuracy of 0.2-0.3 dex. This is the most precise means presently available to predict these sources of emission in lieu of observation. The youngest stars exhibit 0.1 dex scatter, the source of which can be confined to long-term activity cycles, rotational modulation, or an unknown source of variability. We compiled a quick-reference list of available resources for predicting the unobserved UV emission of a star and their distinguishing characteristics in Table 6.

The fits to line evolution with age we have established can be used in models of the photochemical state of an exoplanetary atmosphere at various stellar ages and its evolution through time. Further, they provide a likely bound on the EUV emission of early M stars. Because both the FUV line and X-ray emission of early M stars declines as $t^{-1.3}$, we suggest that EUV emission declines at a similar rate. This is steeper than the rate of decline inferred by King & Wheatley (2020) for K6-M0 stars, but does not alter their conclusion that the bulk of EUV emission occurs after 100 Myr. However, other considerations are likely to make the first 100 Myr of an early M star’s life, when activity is saturated and planetary atmospheres are at their most distended, a critical phase in the atmospheric evolution of orbiting planets. Readers employing our age-evolution fits should bear in mind that order-of-magnitude differences in stellar seed rotation rates can lead to corresponding differences in activity saturation lifetime between individual stars (Tu et al. 2015).

ACKNOWLEDGMENTS

Support for program 14784 was provided by NASA through a grant from the Space Telescope Science Institute (HST-GO-14784.001-A), which is operated by the Association of Universities for Research in Astronomy, Inc., under NASA contract NAS 5-26555. R.O.P.L. and E.S. thank STScI and NASA for this support. We acknowledge with thanks the variable star observations from the AAVSO International Database contributed by observers worldwide and used in this research. The team at STScI were of great help in planning these observations, and we thank them for their responsiveness and attention to detail. Stephanie Douglas and Jason Curtis assisted with determining stellar parameters, including rotation periods and effective temperatures, of the Hyads in the sample, for which we are very grateful. We also wish to thank several scientists who went above and beyond to provide us with extended or more detailed versions of published data products, including George McDonald, who provided posterior distributions for saturation-decay fits; Adam Kraus, who provided optical spectra for possible binary J22025; and Federico Spada, who provided a complete set of stellar isochrones. We are grateful to Ruth Angus, Malodie Kao, Tahina Ramjaramanantsoa, Wilson Cauley, and Ella Osby for helpful advice, questions, and conversations. Anglada-Escudé, C., Tuomi, M., Gerlach, E., et al. 2015, *A&A*, 556, A126

Angus, R., Morton, T., & Foreman-Mackey, D. 2019a, *The Journal of Open Source Software*, 4, 1469
 Angus, R., Morton, T. D., Foreman-Mackey, D., et al. 2019b, *AJ*, 158, 173
 Angus, R., Beane, A., Price-Whelan, A. M., et al. 2020, *AJ*, 160, 90
 Astropy Collaboration, Robitaille, T. P., Tollerud, E. J., et al. 2013, *A&A*, 558, A33
 Astudillo-Defru, N., Delfosse, X., Bonfils, X., et al. 2017, *A&A*, 600, A13
 Avrett, E. H., & Loeser, R. 2008, *ApJS*, 175, 229
 Bailey, J., Butler, R. P., Tinney, C. G., et al. 2009, *ApJ*, 690, 743
 Baraffe, I., & Chabrier, G. 1996, *ApJL*, 461, L51
 Bell, C. P. M., Mamajek, E. E., & Naylor, T. 2015, *MNRAS*, 454, 593
 Björger, J. P., Sukhorukov, A. V., Leenaarts, J., et al. 2018, *A&A*, 611, A62
 Bochanski, J. J., West, A. A., Hawley, S. L., & Covey, K. R. 2007, *AJ*, 133, 531
 Bourrier, V., Lovis, C., Beust, H., et al. 2018, *Nature*, 553, 477
 Brandenburg, A. 2020, arXiv e-prints, arXiv:2004.00439

This research is based on observations made with the NASA/ESA *Hubble Space Telescope*, obtained from the Data Archive at the Space Telescope Science Institute. These observations are associated with program # 14784, with additional data from programs # 12464, 13650, 14767, and 15174. This paper includes data collected with the *TESS* and *Kepler* missions, obtained from the MAST data archive at the Space Telescope Science Institute (STScI). Funding for the TESS mission is provided by the NASA Explorer Program. Funding for the Kepler mission is provided by the NASA Science Mission Directorate. STScI is operated by the Association of Universities for Research in Astronomy, Inc., under NASA contract NAS 5-26555.

Facilities: HST (COS), MAST, K2, TESS, AAVSO, ELODIE, SDSS

Software: isochrone (Morton 2015), astropy (Astropy Collaboration et al. 2013), stardate (Angus et al. 2019a), emcee (Foreman-Mackey et al. 2019), starspot (<https://github.com/RuthAngus/starspot>)

REFERENCES

Brandt, T. D., & Huang, C. X. 2015, *ApJ*, 807, 58
 Butler, R. P., Vogt, S. S., Marcy, G. W., et al. 2004, *ApJ*, 617, 580
 Choi, J., Dotter, A., Conroy, C., et al. 2016, *ApJ*, 823, 102
 Cummings, J. D., Deliyannis, C. P., Maderak, R. M., & Steinhauer, A. 2017, *AJ*, 153, 128
 Curtis, J. L., Agüeros, M. A., Mamajek, E. E., Wright, J. T., & Cummings, J. D. 2019, *AJ*, 158, 77
 Curtis, J. L., Agüeros, M. A., Matt, S. P., et al. 2020, arXiv e-prints, arXiv:2010.02272
 Cutri, R. M., Skrutskie, M. F., van Dyk, S., et al. 2003, 2MASS All Sky Catalog of point sources.
 D’Antona, F., & Mazzitelli, I. 1994, *ApJS*, 90, 467
 Dashtamirova, D., Fischer, W. J., et al., eds. 2020, *Cosmic Origins Spectrograph Instrument Handbook* (Baltimore: STScI). <https://hst-docs.stsci.edu/cosihb>
 Delfosse, X., Forveille, T., Perrier, C., & Mayor, M. 1998, *A&A*, 331, 581
 Dere, K. P., Landi, E., Young, P. R., et al. 2009, *A&A*, 498, 915
 dos Santos, L. A., Bourrier, V., Ehrenreich, D., & Kameda, S. 2019, *A&A*, 622, A46
 Dotter, A. 2016, *ApJS*, 222, 8
 Douglas, S. T., Agüeros, M. A., Covey, K. R., et al. 2016, *ApJ*, 822, 47
 Douglas, S. T., Curtis, J. L., Agüeros, M. A., et al. 2019, *ApJ*, 879, 100

- Feigelson, E. D., Hornschemeier, A. E., Micela, G., et al. 2004, *ApJ*, 611, 1107
- Fontenla, J. M., Linsky, J. L., Witbrod, J., et al. 2016, *ApJ*, 830, 154
- Foreman-Mackey, D., Hogg, D. W., Lang, D., & Goodman, J. 2013, *PASP*, 125, 306
- Foreman-Mackey, D., Farr, W., Sinha, M., et al. 2019, *The Journal of Open Source Software*, 4, 1864
- Forveille, T., Bonfils, X., Delfosse, X., et al. 2009, *A&A*, 493, 645
- France, K., Arulanantham, N., Fossati, L., et al. 2018, *ApJS*, 239, 16
- France, K., Froning, C. S., Linsky, J. L., et al. 2013, *ApJ*, 763, 149
- France, K., Loyd, R. O. P., Youngblood, A., et al. 2016, *ApJ*, 820, 89
- Gaia Collaboration, Brown, A. G. A., Vallenari, A., et al. 2018, *A&A*, 616, A1
- Gaidos, E., Mann, A. W., Lépine, S., et al. 2014, *MNRAS*, 443, 2561
- Green, J. C., Froning, C. S., Osterman, S., et al. 2012, *ApJ*, 744, 60
- Guinan, E. F., Ribas, I., & Harper, G. M. 2003, *ApJ*, 594, 561
- Henry, T. J., Jao, W.-C., Winters, J. G., et al. 2018, *AJ*, 155, 265
- Hu, R., Seager, S., & Bains, W. 2012, *ApJ*, 761, 166
- Jackson, A. P., Davis, T. A., & Wheatley, P. J. 2012, *MNRAS*, 422, 2024
- Johnstone, C. P., Bartel, M., & Güdel, M. 2020, *arXiv e-prints*, arXiv:2009.07695
- Kasting, J. F., Whitmire, D. P., & Reynolds, R. T. 1993, *Icarus*, 101, 108
- Kim, Y.-C., & Demarque, P. 1996, *ApJ*, 457, 340
- King, G. W., & Wheatley, P. J. 2020, *arXiv e-prints*, arXiv:2007.13731
- King, G. W., Wheatley, P. J., Salz, M., et al. 2018, *MNRAS*, 478, 1193
- Kopparapu, R. K., Ramirez, R., Kasting, J. F., et al. 2013, *ApJ*, 765, 131
- Kraus, A. L., Shkolnik, E. L., Allers, K. N., & Liu, M. C. 2014, *AJ*, 147, 146
- Leenaarts, J., Pereira, T. M. D., Carlsson, M., Uitenbroek, H., & De Pontieu, B. 2013, *ApJ*, 772, 89
- Linsky, J. L., Bushinsky, R., Ayres, T., Fontenla, J., & France, K. 2012, *ApJ*, 745, 25
- Linsky, J. L., Yang, H., France, K., et al. 2010, *ApJ*, 717, 1291
- Linsky, J. L., Wood, B. E., Youngblood, A., et al. 2020, *ApJ*, 902, 3
- Lopez, E. D., & Fortney, J. J. 2013, *ApJ*, 776, 2
- Loyd, R. O. P., Shkolnik, E. L., Schneider, A. C., et al. 2018a, *ApJ*, 867, 70
- Loyd, R. O. P., France, K., Youngblood, A., et al. 2016, *ApJ*, 824, 102
- . 2018b, *ApJ*, 867, 71
- Luger, R., Barnes, R., Lopez, E., et al. 2015, *Astrobiology*, 15, 57
- Maeder, A., & Mermilliod, J. C. 1981, *A&A*, 93, 136
- Mann, A. W., Feiden, G. A., Gaidos, E., Boyajian, T., & von Braun, K. 2015, *ApJ*, 804, 64
- Martín, E. L., Lodieu, N., Pavlenko, Y., & Béjar, V. J. S. 2018, *ApJ*, 856, 40
- McDonald, G. D., Kreidberg, L., & Lopez, E. 2019, *ApJ*, 876, 22
- McQuillan, A., Aigrain, S., & Mazeh, T. 2013, *MNRAS*, 432, 1203
- Melbourne, K., Youngblood, A., France, K., et al. 2020, *arXiv e-prints*, arXiv:2009.07869
- Messina, S., Desidera, S., Lanzafame, A. C., Turatto, M., & Guinan, E. F. 2011, *A&A*, 532, A10
- Messina, S., Desidera, S., Turatto, M., Lanzafame, A. C., & Guinan, E. F. 2010, *A&A*, 520, A15
- Miles, B. E., & Shkolnik, E. L. 2017, *AJ*, 154, 67
- Morton, T. D. 2015, *isochrones: Stellar model grid package*, , ascl:1503.010
- Moultaka, J., Ilovaisky, S. A., Prugniel, P., & Soubiran, C. 2004, *PASP*, 116, 693
- Mulders, G. D. 2018, *Planet Populations as a Function of Stellar Properties*, 153
- Murray-Clay, R. A., Chiang, E. I., & Murray, N. 2009, *ApJ*, 693, 23
- Newton, E. R., Irwin, J., Charbonneau, D., et al. 2016, *ApJ*, 821, 93
- Newton, E. R., Mondrik, N., Irwin, J., Winters, J. G., & Charbonneau, D. 2018, *AJ*, 156, 217
- Noyes, R. W., Hartmann, L. W., Baliunas, S. L., Duncan, D. K., & Vaughan, A. H. 1984, *ApJ*, 279, 763
- Oelkers, R. J., Rodriguez, J. E., Stassun, K. G., et al. 2018, *AJ*, 155, 39
- Owen, J. E., & Wu, Y. 2013, *ApJ*, 775, 105
- . 2017, *ApJ*, 847, 29
- Pagano, I., Linsky, J. L., Carkner, L., et al. 2000, *ApJ*, 532, 497
- Peacock, S., Barman, T., Shkolnik, E. L., et al. 2019, *ApJ*, 886, 77
- . 2020, *ApJ*, 895, 5
- Perryman, M. A. C., Brown, A. G. A., Lebreton, Y., et al. 1998, *A&A*, 331, 81

- Pizzolato, N., Maggio, A., Micela, G., Sciortino, S., & Ventura, P. 2003, *A&A*, 397, 147
- Preibisch, T., & Feigelson, E. D. 2005, *ApJS*, 160, 390
- Redfield, S., & Linsky, J. L. 2002, *ApJS*, 139, 439
- Ribas, I., Guinan, E. F., Güdel, M., & Audard, M. 2005, *ApJ*, 622, 680
- Richey-Yowell, T., Shkolnik, E. L., Schneider, A. C., et al. 2019, *ApJ*, 872, 17
- Schneider, A. C., & Shkolnik, E. L. 2018, *AJ*, 155, 122
- Segura, A., Kasting, J. F., Meadows, V., et al. 2005, *Astrobiology*, 5, 706
- Shkolnik, E. L., & Barman, T. S. 2014, *AJ*, 148, 64
- Spada, F., & Lanzafame, A. C. 2020, *A&A*, 636, A76
- Stauffer, J. R., Balachandran, S. C., Krishnamurthi, A., et al. 1997, *ApJ*, 475, 604
- Stelzer, B., Marino, A., Micela, G., López-Santiago, J., & Liefke, C. 2013, *MNRAS*, 431, 2063
- . 2014, *MNRAS*, 442, 343
- Suárez Mascareño, A., Rebolo, R., González Hernández, J. I., & Esposito, M. 2015, *MNRAS*, 452, 2745
- Tabernerero, H. M., Montes, D., & González Hernández, J. I. 2012, *A&A*, 547, A13
- Torres, C. A. O., Quast, G. R., da Silva, L., et al. 2006, *A&A*, 460, 695
- Torres, G., Winn, J. N., & Holman, M. J. 2008, *ApJ*, 677, 1324
- Tu, L., Johnstone, C. P., Güdel, M., & Lammer, H. 2015, *A&A*, 577, L3
- von Braun, K., Boyajian, T. S., van Belle, G. T., et al. 2014, *MNRAS*, 438, 2413
- Watson, C. L., Henden, A. A., & Price, A. 2006, *Society for Astronomical Sciences Annual Symposium*, 25, 47
- Wedemeyer, S., Freytag, B., Steffen, M., Ludwig, H. G., & Holweger, H. 2004, *A&A*, 414, 1121
- West, A. A., Hawley, S. L., Bochanski, J. J., et al. 2008, *AJ*, 135, 785
- Wittenmyer, R. A., Tuomi, M., Butler, R. P., et al. 2014, *ApJ*, 791, 114
- Wright, N. J., Drake, J. J., Mamajek, E. E., & Henry, G. W. 2011, *ApJ*, 743, 48
- Wright, N. J., Newton, E. R., Williams, P. K. G., Drake, J. J., & Yadav, R. K. 2018, *MNRAS*, 479, 2351
- Youngblood, A., France, K., Loyd, R. O. P., et al. 2016, *ApJ*, 824, 101
- . 2017, *ApJ*, 843, 31
- Zacharias, N., Finch, C. T., Girard, T. M., et al. 2012, *VizieR Online Data Catalog*, I/322A

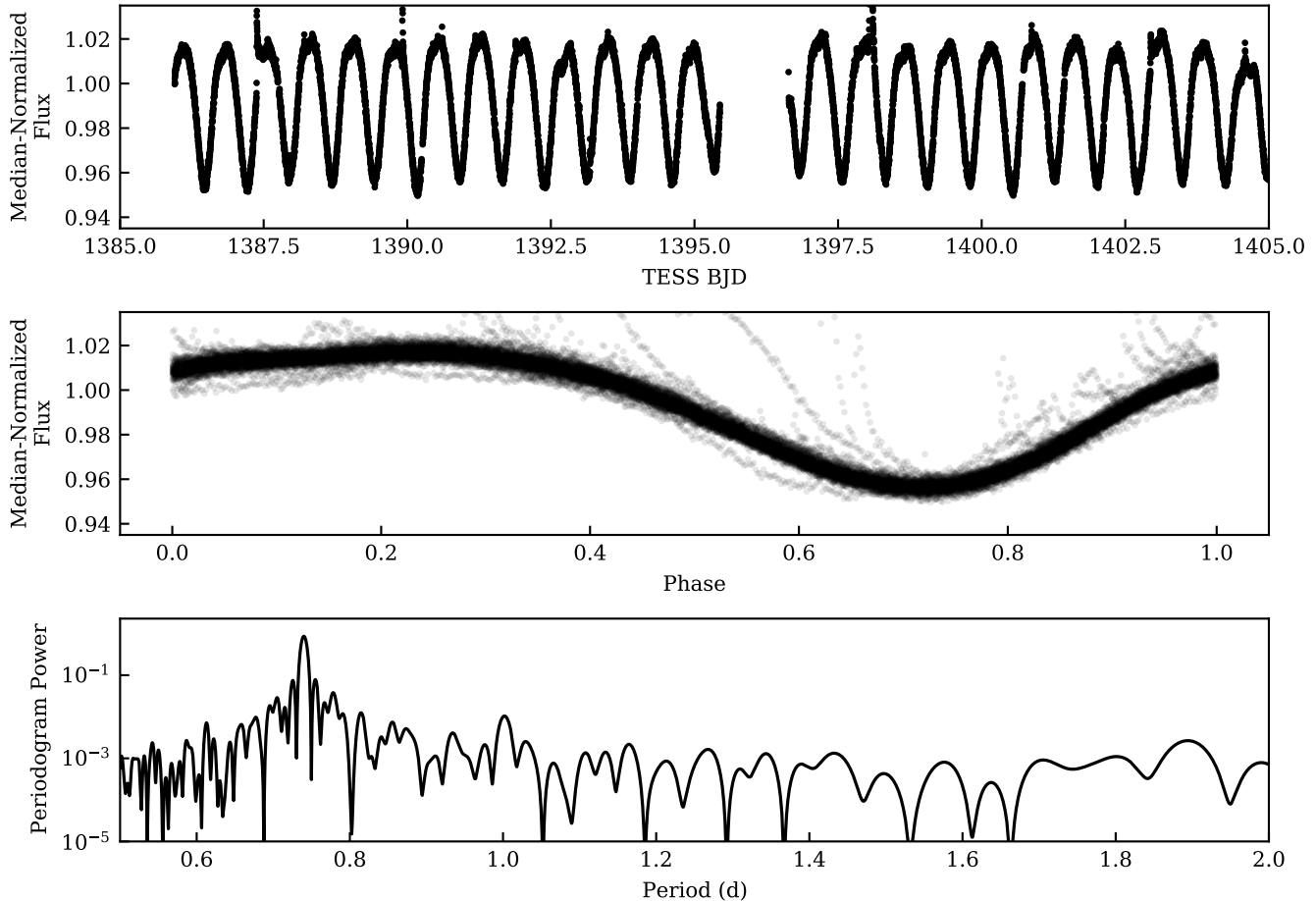


Figure 9. *TESS* lightcurve and Lomb-Scargle periodogram for J02365. The top panel shows one sector of the *TESS* data. The middle panel shows the data from both sectors folded on the period of maximum power. Positive excursions, some off the plot range, are stellar flares. The bottom panel shows the results of the periodogram analysis with a strong peak at 0.74 d.

APPENDIX

A. CUSTOM COADDITION OF SPECTRA

To coadd spectra obtained using different central wavelength settings, we first established a common wavelength grid covering all wavelengths where at least one spectrum had data at the same resolution as the component spectra. We then rebinned each spectrum onto this wavelength grid ensuring that total flux was preserved. Once rebinned, we averaged fluxes and errors (in quadrature), weighting by exposure time. We masked data in pixels flagged with data quality issues marked as serious within the x1d file headers. If this resulted in no data in a pixel, then we retained the flagged data. We propagated all data quality flags for masking in later fits.

B. PERIODOGRAM FOR J02365

Because several rotation periods have been reported in the literature for J02365, we here provide a diagnostic figure for our periodogram analysis (Figure 9). This may also serve as an example for other stars for which we derived rotation periods from *TESS* data.